The Ketogenic Diet Metabolite β-Hydroxybutyrate Promotes Mitochondrial Elongation via Deacetylation and Improves Autism-like Behavior in Zebrafish

Golam M. Uddin[1,3,5], Rachel Lacroix[1,3,4,5], Mashiat Zaman[1,2,3,4], Iman Al Khatib[1,3,5], Amit Jaiswal[1,2,3,4] Jong M. Rho[7], Deborah M. Kurrasch[1,3,4,6], Timothy E. Shutt [1,2,3,4,5,6 *]

[1] Cumming School of Medicine, University of Calgary, Calgary, AB, Canada

[2] Department of Biochemistry and Molecular Biology, University of Calgary, Calgary, AB, Canada

[3] Alberta Children's Hospital Research Institute (ACHRI), Calgary, AB, Canada

[4] Hotchkiss Brain Institute, University of Calgary, Calgary, AB, Canada

[5] Snyder Institute for Chronic Diseases, University of Calgary, Calgary, AB, Canada

[6] Department of Medical Genetics, University of Calgary, Calgary, AB, Canada

[7] Departments of Pediatrics, Yale School of Medicine, Yale University, New Haven, CT, USA

Address for Correspondence:

Corresponding Author

Dr. Timothy Shutt

Associate Professor

Email: timothy.shutt@ucalgary.ca

Phone: +1 (403)-220-6114

Abstract

The ketogenic diet (KD) is clinically beneficial and has therapeutic potential across a growing list of neurological disorders, including autism spectrum disorder (ASD). However, the underlying mechanisms mediating the benefits of the KD, which can also have undesirable side effects, remain undefined. To this end, improvements in mitochondrial morphology and function correlate with improved ASD behaviours in response to the KD, though how the KD influences mitochondrial morphology, and whether this is sufficient to improve behaviour remains unknown. Here, we investigate how beta-hydroxybutyrate (BHB), a key metabolite produced by the KD regulates mitochondrial morphology, and whether this pathway could be exploited to alter phenotypes in a zebrafish model of ASD. We found that β-oxidation of BHB promotes mitochondrial elongation by increasing NAD^+ levels, which in turn activates SIRT deacetylases that act on key regulators of both mitochondrial fusion and fission. Our data suggest that increasing NAD^+ levels with its precursor, nicotinamide nucleotide (NMN), is sufficient to promote mitochondrial hyperfusion. Finally, both BHB and NMN impact neurodevelopment in the *shank3b*$^{+/-}$ zebrafish model of ASD. Together, our findings elucidate a mechanism by which the ketogenic diet promotes mitochondrial elongation. Moreover, manipulation of this pathway may provide a novel avenue for the treatment of neurological disorders such as ASD that also may obviate potential complications of the KD in clinical practice.

Introduction:

The high-fat low-carbohydrate ketogenic diet (KD), long appreciated for its clinical efficacy for epilepsy (Neal et al., 2008), is also recognized to have potential beneficial effects in a growing list of diseases. The KD appears beneficial in neurodevelopmental disorders such as autism spectrum disorder (ASD) (Gogou & Kolios, 2018; Napoli et al., 2014), as well as in neurodegenerative diseases such as amyotrophic lateral sclerosis (Zhao et al., 2006), Parkinson disease and Alzheimer disease (Kashiwaya et al., 2000). For example, in the 3xTgAD mouse model of Alzheimer disease, the KD or ketone esters ameliorated AD pathogenesis, improved cognitive function and reduced anxiety. Moreover, due to its ability to manipulate mitochondrial energy metabolism, the KD may also be effective against cardiovascular diseases (Lopaschuk et al., 2020), or as a cancer treatment (Weber et al., 2020). Despite the well-documented benefits of the KD, concerns about limitations and complications of the diet are worth noting. For example, compliance with the KD can be challenging, especially in children and adolescents (Lin et al., 2017), with gastrointestinal side effects (39%) such as nausea/vomiting (28%), diarrhea (33%), constipation (2%), as well as hypertriglyceridemia (27%) being reported in patients (Kang et al., 2004). Understanding how the KD works will facilitate the development of alternative approaches that could avoid these complications.

Mitochondria are thought to be a central target mediating the effects of the KD. A key aspect regulating mitochondrial function is their dynamic structure, as they capable of fusing, dividing, and moving about the cell (Shutt & McBride, 2013; Wai & Langer, 2016). These processes influence mitochondrial function, with fragmentation of the

mitochondrial network often associated with dysfunction (Baker et al., 2019; Glancy et al., 2020). Notably, recent work has shown that the KD can improve mitochondrial structure and function in the BTBR mouse model of ASD (Ahn et al., 2020), which is consistent with behavioral benefits in mouse models of ASD (Ahn et al., 2014; Ruskin et al., 2017; Ruskin et al., 2013), and clinical trials in children (El-Rashidy et al., 2017; Evangeliou et al., 2003; R. W. Y. Lee et al., 2018). However, the underlying mechanism(s) by which KD regulates mitochondrial structure remain unclear.

The ketone body β-hydroxybutyrate (BHB) is a key metabolic product of the KD that is thought to mediate many of the therapeutic effects of the KD (Newman & Verdin, 2017). There are multiple ways through which BHB is proposed to act, including inhibition of histone deacetylases that can elicit changes in gene expression (Shimazu et al., 2013), acting as a signaling molecule via G-protein-coupled receptors (GPCR) (Miyamoto et al., 2019), and as a metabolite consumed by mitochondria to generate ATP. With respect to this latter mechanism, when mitochondria catabolise BHB via β-oxidation instead of glucose, more NAD^+ is available, with less being converted to NADH (Elamin et al., 2017; Newman & Verdin, 2017). Given that NAD^+ is a necessary cofactor in several important enzymatic reactions, BHB-mediated changes in NAD^+ can impact many cellular and mitochondrial functions. For example, NAD^+ activates the sirtuin deacetylase enzymes (SIRTs) (Bonkowski & Sinclair, 2016; Covarrubias et al., 2021), which is a notable phenomenon since protein deacetylation can mediate mitochondrial elongation (Uddin et al., 2021). Indeed, an early report linking BHB to NAD+ metabolism found a high-fat diet was beneficial in a model of premature aging due elevated levels of BHB and activation SIRT1 (Scheibye-Knudsen et al., 2014) While

NAD+ augmentation mirrored the benefits of the high fat diet, a link between BHB and increased NAD+ levels was not established at that time.

Mitochondrial dynamics, encompassing fusion, fission, mitophagy, and interactions with other organelles, are key aspects of maintaining mitochondrial function (Uddin, Abbas, & Shutt, 2021). Fusion and fission events allow mitochondria to adapt to the cell's metabolic demands and impact mitochondrial morphology, cristae structure, energy production, apoptosis susceptibility, and mitochondrial quality control. Notably, NAD+ supplementation promotes mitophagy, which is crucial for mitochondrial maintenance (Fang et al., 2014; Gilmour et al., 2020). Meanwhile, NAD+ is a critical metabolite in the brain, where we also know mitochondrial function and mitochondrial dynamics are important, as NAD+ depletion is implicated in a growing list of neurodegenerative disorders (Fang et al., 2019). Understanding the intricate interplay between NAD+, protein acetylation, and mitochondrial dynamics is crucial for unraveling the mechanisms underlying mitochondrial dysfunction and exploring potential therapeutic interventions for related diseases.

Zebrafish are a valuable model for studying complex brain disorders such as ASD (Kalueff et al., 2014). Recently, genetic mutant models of verified autism-risk genes have been created and are shown effectively recapitulate autism-like behaviours (Durand et al., 2007; Liu et al., 2018). *SHANK3* encodes a master scaffolding protein that has critical roles in synaptogenesis and synaptic function (Monteiro & Feng, 2017), and is a validated ASD-risk gene in humans (SFARI, 2022; Yi et al. 2016). Moreover, *shank3b*$^{+/-}$ deficient zebrafish display core features of ASD-like behaviour, such as impaired locomotor activity, repetitive behaviours and social defects (S. Lee et al., 2018;

Liu et al., 2018). Linking SHANK3 to mitochondria and mitochondrial function, mouse models show that the SHANK3 protein interacts with several mitochondrial proteins (Lee et al., 2017). Meanwhile, mice harboring a *Shank3* mutation associated with ASD had elevated S-nitrosylation of mitochondrial proteins, indicative of mitochondrial dysfunction (Kartawy et al., 2021).

While BHB treatment leads to mitochondrial elongation in cultured cells (Ahn et al., 2020; Santra et al., 2004), it is neither clear how BHB regulates mitochondrial morphology, nor whether BHB alone is sufficient to recapitulate the beneficial effects of the KD on ASD behaviours. Here, we investigated if and how mitochondrial morphology is impacted by BHB-mediated changes in NAD^+, and whether this pathway could potentially be exploited to improve behaviors in a zebrafish model of ASD.

Results

BHB mediated increase in NAD^+ is necessary to promote mitochondrial elongation:

Building on previous work showing that BHB induces mitochondrial elongation in primary neuronal cultures (Ahn et al., 2020), we wanted to examine the mechanistic underpinnings of BHB-induced mitochondrial elongation in HeLa cells, a standard cell culture model that is often used to study mitochondrial dynamics as it is easy to work with and to visualize mitochondrial morphology. An initial dose response showed that a 24 hr treatment with BHB induces mitochondrial elongation in HeLa cells (Supplemental Fig 1). We chose to use the 5 mM dose as our treatment paradigm since this dose had the strongest effect on morphology and is a physiologically relevant dose for ketone levels found with the ketogenic diet. A more detailed analysis of mitochondrial morphology showed that 24 hr treatment with 5 mM BHB promoted mitochondrial elongation in HeLa cells (Figure 1A), as assessed by both quantitative analysis of mitochondrial branch length (Figure 1B), and qualitative analysis of overall mitochondrial morphology via visual scoring (Figure 1C). In conjunction with mitochondrial elongation, BHB treatment also increased basal oxygen consumption (Supplemental Fig 2). As BHB is reported to increase NAD^+ via β-oxidation (Elamin et al., 2017), we measured levels of NAD^+ in BHB-treated cells. As expected, treatment with BHB increased the levels of NAD^+ (Figure 1D, Supplementary figure 3B and 4D) and NAD^++ NADH levels (Supplementary Figure 3C and 4E). Notably, blocking β-oxidation using the CPT1a inhibitor etomoxir (Xu et al., 2003) prevented both BHB-mediated increases in NAD^+ (Figure 1D) and mitochondrial elongation (Figure 1A-C,

Supplemental Figure 4A-C), suggesting that β-oxidation is required for BHB to increase NAD^+ levels, and that increased NAD^+ is required for BHB-induced mitochondrial elongation.

Increased NAD^+ is sufficient to promote mitochondrial elongation:

To investigate whether increased NAD^+ alone could promote mitochondrial elongation, we treated cells with the NAD^+ precursor molecule nicotinamide mononucleotide (NMN). Similar to the BHB treatment, we found that the NMN can increase both NAD^+ levels (Figure 1D) and NAD^++ NADH levels (Supplementary Figure 3C), as well as promote mitochondrial elongation (Figure 1A-C).

BHB and NMN promote mitochondrial elongation by increasing mitochondrial fusion and decreasing mitochondrial fission:

Mitochondrial elongation can be caused by either increased fusion and/or decreased fission (Sabouny & Shutt, 2020). To investigate how BHB and NMN promote mitochondrial elongation, we examined key proteins mediating both mitochondrial fusion and fission (Figure 2A-D, Supplemental Figure 3D-G). We found that expression of the OPA1 fusion protein was increased significantly by treatment with BHB, but not NMN. Meanwhile, both BHB and NMN treatments reduced phosphorylation of DRP1 at position serine-616, which is a well-characterized post-translational modification that promotes mitochondrial fission (Sabouny & Shutt, 2020; Uddin et al., 2021). Notably, we did not see any significant changes due to BHB or NMN treatment in DRP1

phosphorylation at serine-637, which inhibits mitochondrial fission (Sabouny & Shutt, 2020; Uddin et al., 2021), nor in the total expression of other key mitochondrial fusion (MFN1, MFN2) or fission (MFF) proteins (Supplementary Figure 3D-G).

As peroxisomes share the same fission machinery with mitochondria, but do not undergo fusion with one another, we next examined if BHB and NMN also impacted peroxisomal morphology through inhibition of peroxisome fission. Curiously, while BHB supplementation increases peroxisome size, NMN supplementation had no effect, suggesting that any effects of BHB on peroxisome morphology was independent of NAD^+ (Fig 2E-F). Supporting this notion, blocking β-oxidation with etoxomir treatment did not impact BHB-induced enlargement of peroxisomes. We also noted that BHB, but not NMN, induced a marked increase in the number of peroxisomes (Fig 2G), consistent with a role for BHB in promoting peroxisome biogenesis independent of its NAD^+-mediated effects.

Next, we interrogated protein acetylation since increased NAD^+ promotes protein deacetylation, a post-translational modification linked to changes in mitochondrial morphology (Uddin et al., 2021). Notably, deacetylation of mitochondrial fusion proteins MFN1, MFN2, and OPA1 is reported to promote mitochondrial fusion (Biel et al., 2016; Lee et al., 2014; Samant et al., 2014), while deacetylation of DRP1 is linked to decreased fission (Hu et al., 2020). As expected, we found that BHB and NMN both reduce global protein acetylation (Figure 3A and B). More specifically, we observed decreased acetylation of OPA1 and DRP1 (Figure 3A, C and D), but were unable to detect any acetylation of MFN1/ MFN2 proteins.

BHB and NMN control mitochondrial morphology via sirtuin-based deacetylation activity:

To determine if NAD^+-mediated protein deacetylation is important for promoting mitochondrial elongation induced by BHB and NMN, and whether sirtuin deacetylases are involved, we examined the effects of sirtinol, an inhibitor of both Sirt1 and Sirt2 (Mai et al., 2005). Treatment with 50 µM sirtinol increased global acetylation (Supplementary Figure 4 G-H) and caused an accumulation of NAD^+ (Supplementary Figure 4I), indicating that the inhibitor was functional. Sirtinol treatment also led to fragmentation of the mitochondrial network (Figure 4A-C), consistent with increased protein acetylation levels correlating to mitochondrial fragmentation. Critically, sirtinol treatment prevented BHB and NMN-induced mitochondrial elongation (Figure 4A-C), implicating a role for Sirt1 and/or Sirt2 in BHB and NMN-induced mitochondrial elongation.

Sirt2 is required for NAD^+ induced mitochondrial elongation via BHB:

To determine if Sirt1, Sirt2, and/or Sirt3 is required for BHB or NMN induced mitochondrial elongation, their expression was knocked down separately via siRNA (Figure 5, Supplementary Figure 3-5). To control for off-target effects, we used three different siRNA targets for each gene and confirmed knockdown via western blotting (Figure 5D). Upon examining mitochondrial morphology, we observed a similar trend of mitochondrial fragmentation for 2 of the 3 siRNA targets for Sirt1(siRNA#1&2), Sirt2 (siRNA#2&3) and Sirt3 (siRNA#1&3) (Supplemental Figures 5, 6 and 7), again consistent with the notion that deacetylation promotes mitochondrial elongation. Since

the results from Sirt1 siRNA#3, Sirt2 siRNA#1 and Sirt3 siRNA#2 were not consistent (possibly due to off-target effects), they were discarded from our interpretation. Overall, we found that BHB-induced mitochondrial elongation was unaffected by Sirt1 and Sirt3 knock-down, but was abolished by Sirt2 knock-down. Meanwhile, knock-down of either Sirt1 or Sirt2 prevented an NMN-induced mitochondrial hyperfusion phenotype, while Sirt3 knock-down had no effect. However, it should be noted that Sirt3 knockdown was less efficient, and that there could still be residual protein activity. Together, our findings indicate that Sirt2 is required for both BHB- and NMN-induced mitochondrial elongation via increased NAD^+ levels. Meanwhile, the fact that BHB, but not NMN, can induce mitochondrial elongation in the absence of Sirt1 suggests that BHB can also induce mitochondrial elongation via an NAD^+-independent mechanism, consistent with the fact that BHB, but not NMN, increased OPA1 expression.

BHB and NMN impact behaviours in a *shank3b*$^{+/-}$ zebrafish model of ASD:

To examine the efficacy of BHB or NMN *in vivo* for the potential treatment of ASD, we studied their effects in *shank3b*$^{+/-}$ zebrafish. Wild-type siblings and s*hank3b*$^{+/-}$ fish were exposed to vehicle, BHB, or NMN over the neurogenic developmental timepoint (10-48 hpf (hour post fertilization); Figure 6A). When fish begin to move at 5 dpf (day post fertilization), locomotor behaviours were examined by measuring total movement in the light and the dark (Figure 6). Specifically, *shank3b*$^{+/-}$ fish showed reduced distance travelled in both dark (Figure 6C) and light (Figure 6D); $p<0.0001$) compared to *shank3b*$^{+/+}$ (wild-type) fish exposed to vehicle. Despite a reduced distance travelled, the average speed of *shank3b*$^{+/-}$ fish was increased in both light and dark

conditions (Fig 6E,F). In *shank3b*$^{+/-}$ fish, BHB restored distance travelled in light and dark conditions to the levels of wild-type control fish, while there was no difference between the speed of *shank3b*$^{+/-}$ and wild-type exposed to BHB. NMN restored distance travelled by *shank3b*$^{+/-}$ in light to wild-type levels, while in the dark the distance travelled was similar in both *shank3b*$^{+/-}$ and wild-type. The speed of NMN exposed fish was the same in the light and *shank3b*$^{+/-}$ fish moved faster in the dark.

In addition to standard movement parameters such as distance travelled and speed, we also examined the thigmotaxis, which is the behavioral response to remain close to walls and can be a measure of anxiety. In control conditions, wild-type fish spend more time in the peripheral region near the walls compared to *shank3b*$^{+/-}$ fish. However, following exposure to BHB, both wild-type and *shank3b*$^{+/-}$ fish spend the same time in the peripheral region. Meanwhile following NMN exposure, *shank3b*$^{+/-}$ fish spend more time peripherally than wild-type fish. As such, both BHB and NMN reverse the thigmotaxis differences observed in *shank3b*$^{+/-}$ fish.

These findings suggests that either treatment is effective in restoring movement and thigmotaxis to or above the baseline of wild-type, vehicle exposed fish. Unexpectedly, we observed that BHB alone had an effect in wild-type fish under light conditions, significantly decreasing locomotion compared to vehicle-exposed controls (Figure 6D). This decrease was not observed in wild-type fish exposed to NMN, suggesting differences in the mechanism(s) through which BHB and NMN elicit their effects. Along these lines, NMN had more dramatic effects on thigmotaxis and standard movement. Nonetheless, these findings indicate that the movement and thigmotaxis

phenotypes in *shank3b*$^{+/-}$ zebrafish were restored upon developmental exposure to either BHB or NMN.

BHB and NMN impact bioenergetics in a *shank3b*$^{+/-}$ zebrafish:

We also examined bioenergetics in wild-type and *shank3b*$^{+/-}$ fish, and the impact of BHB. At 2 dpf, at the end of the exposure phase, single zebrafish were assessed for bioenergetics using the Seahorse Bioanalyzer to measure oxygen consumption rate (OCR) and extracellular flux (ECAR), basally and in response to various mediators of oxidative phosphorylation (Fig 7). No significant differences were observed in basal respiration upon treatment with oligomycin to block the ATPase or with FCCP treatment to uncouple mitochondria. Of note, upon antimycin A treatment to block complex III and flux through the electron transport chain, *shank3b*$^{+/-}$ fish had reduced OCR, indicative of lower non-mitochondrial respiration. However, treatment with BHB rescued this deficit. For ECAR, the only difference between wild-type and *shank3b*$^{+/-}$ fish was observed with antimycin A, with *shank3b*$^{+/-}$ fish showing a reduction. Upon BHB treatment, no difference between wild-type and *shank3b*$^{+/-}$ fish was observed; however, this change appears to be largely due to a decrease in the ECAR in BHB-treated wild-type fish.

Discussion

Our findings provide novel insights into the mechanism by which the KD promotes mitochondrial elongation and suggest that this pathway might be a promising avenue for improving ASD behaviours. The data herein support a model by which β-oxidation of the KD metabolite BHB increases NAD^+ levels to activate sirtuins, which in

turn deacetylate key mitochondrial dynamics proteins to promote mitochondrial hyperfusion.

Pathways that modulate mitochondrial morphology often act reciprocally on both fission and fusion, such that mitochondrial hyperfusion is a result of both decreased fission and increased fusion (Sabouny & Shutt, 2020). This situation is true in response to decreased acetylation (Uddin et al., 2021), and our data show this is mirrored by BHB and NMN treatments. With respect to increased fusion, both BHB and NMN reduced OPA1 acetylation, which promotes mitochondrial fusion (Samant et al., 2014; Sheng & Cristea, 2021). While previous work has shown that deacetylation also activates mitochondrial fusion proteins MFN1 and MFN2 (Lee et al., 2014; Oanh et al., 2017), we were unable to detect acetylation of these proteins to see how they behaved. Meanwhile, both BHB and NMN also reduced DRP1 acetylation, which is known to reduce fission (Hu et al., 2020). Though the mechanism by which deacetylation reduces fission is unknown, it is tempting to speculate that the acetylation status of DRP1 influences the pro-fission phosphorylation at serine-616 of DRP1. This notion is supported by reduced levels of $DRP1^{P616}$ with both BHB and NMN treatments in this study, and previous work showing NMN treatment decreased $DRP1^{P616}$ in mice hippocampal tissues (Hu et al., 2020; Klimova et al., 2019), as well as our previous findings of reduced $DRP1^{P616}$ in mouse brains following 2 weeks on the KD (Ahn et al., 2020).

To further investigate the mechanistic pathway by which NAD^+ mediates deacetylation of proteins mediating mitochondrial dynamics, we interrogated the role of Sirt1 and Sirt2, which both localize to the cytosol where they can act on DRP1, as well

as Sirt3, which localizes inside of mitochondria where it can act on OPA1. While Sirt3 knockdown did not affect either BHB or NMN-mediated hyperfusion, it is notable that we did not achieve a high reduction in Sirt3 protein levels, and that residual Sirt3 protein could still be active. Meanwhile, knockdown of both Sirt1 and Sirt2 prevented NMN-induced mitochondrial hyperfusion, while only Sirt2 knockdown inhibited BHB-induced mitochondrial hyperfusion. This discrepancy could be due to the fact that BHB has multiple mechanisms of action beyond the novel pathway we have shown here for protein deacetylation via NAD^+ and sirtuins (Newman & Verdin, 2014).

In this regard, we also observed other notable differences between BHB and NMN treatments. First, while BHB increased OPA1 protein levels, NMN did not. This observation is similar to previous work in mouse hippocampal tissues where NMN elevated NAD^+ levels but did not change OPA1 expression (Klimova et al., 2019). Given that NMN increases NAD^+ levels, but not total OPA1 protein, we suggest that the elevated OPA1 expression from BHB supplementation is independent of NAD^+ changes. Another difference between BHB and NMN was with respect to peroxisome morphology, which was investigated because mitochondria and peroxisomes share the same fission machinery. We propose that the increased peroxisome size and abundance with BHB treatment is likely due to the BHB induction of peroxisome proliferator-activated receptors (PPARs), rather than increased NAD^+. This conclusion is based on the observations that etomoxir did not prevent BHB-induced peroxisome elongation, and that NMN had no effect on peroxisome size. Moreover, BHB-induced increases in peroxisome abundance would be consistent with the known role of PPARs in promoting peroxisome biogenesis and activating β-oxidation (Dreyer et al., 1993;

Hess et al., 1965). This alternative pathway likely involves the ability of BHB to inhibit histone deacetylases HDAC1, 3 and 4 (Newman & Verdin, 2014; Shimazu et al., 2013), as HDAC3 inhibition activates PPARγ (Galmozzi et al., 2013).

The finding that changes in global acetylation and decreased levels of DRP1^{P616} do not impact peroxisome fission was somewhat unexpected, given the role of DRP1 in the fission of both these organelles. However, this finding is consistent with recent work showing that loss of CLUH did not affect peroxisomal fission despite reducing mitochondrial recruitment of DRP1 and mitochondrial fission (Yang et al., 2022). These unexpected observations suggest that there are discrepancies in how DRP1 regulation impacts both mitochondrial and peroxisomal fission, with DRP1^{S616} affecting mitochondrial fission, but not peroxisome fission

While inhibiting mitochondrial fission or improving mitochondrial fusion alone can improve mitochondrial function in several preclinical disease models (Whitley et al., 2019), it is important to note that we see global decreases in protein deacetylation, not just for mitochondrial fission and fusion proteins. Thus, the benefits of promoting protein deacetylation likely go beyond promoting mitochondrial hyperfusion. Additionally, it should be noted that NAD^+ is a critical cofactor for many additional important enzymes that could also contribute to improving mitochondrial function. Consistent with this notion, NAD^+ supplementation is emerging as a popular therapeutic strategy in many diseases (Bonkowski & Sinclair, 2016; Gilmour et al., 2020; Uddin et al., 2021).

There is growing evidence that mitochondrial dysfunction, which often correlates with mitochondrial fragmentation, is likely to contribute to ASD (Citrigno et al., 2020;

Pecorelli et al., 2020; Rossignol & Frye, 2012; Singh et al., 2020; Thorsen, 2020; Weissman et al., 2008). For example, ASD patient cells (Barone et al., 2021; Frye et al., 2021; Gevezova et al., 2021) and brain organoids (Ilieva et al., 2022) exhibit impaired mitochondrial bioenergetics, while postmortem brains of control and ASD patients have increased expression of mitochondrial fission proteins and decreased expression of mitochondrial fusion proteins (Tang et al., 2013). This correlation is also present in animal models of ASD, as neuronal mitochondria in the BTBR mouse model of ASD have reduced mitochondrial function and are more fragmented (Ahn et al., 2020). However, despite the benefits of the KD for ASD behaviors in human studies (El-Rashidy et al., 2017; Spilioti et al., 2013) and in animal models (Y. Ahn et al., 2020), we do not as yet fully understand how the KD provides these benefits, as it has many potential modes of action. Nonetheless, the observation that *shank3b*$^{+/-}$ fish have subtle alterations in bioenergetics, which are restored with BHB exposure, is consistent with a role for mitochondrial dysfunction contributing to ASD. It should be noted that we measured bioenergetics of the whole fish, not the brain specifically; however, our previous studies showed no difference in bioenergetic readouts when measured from whole larval zebrafish or just a dissected head (Ibhazehiebo et al, Brain, 2018), suggesting that the large energy demands of the brain mask any peripheral mitochondrial contributions at this time point.

Our finding that either BHB or NMN improve the locomotion and thigmotaxis behaviours of *shank3b*$^{+/-}$ fish, begins to provide insight into the mechanisms underlying the benefits of the KD, and is noteworthy for several reasons. First, the observation that BHB alone is beneficial suggests that administration of the full KD may not be

necessary. Second, the finding that NMN alone is beneficial suggests that the ability of BHB to increase NAD^+ is important for its benefits. Third, the observation that there are some differences in the effects of BHB and NMN, both at the cellular level and at the behavioural level, suggests that BHB has additional mechanisms of action beyond increasing NAD^+ that may also impact behaviour. In this regard, it might be interesting to examine the combined effects of BHB and NMN. Finally, if the benefits of BHB or NMN in *shank3b*$^{+/-}$ fish are translatable to humans, then administration of BHB or NMN could be a promising approach that bypasses many of the side effects of the KD. However, while it is tempting to propose BHB or NAD+ boosting treatments for ASD, it should be noted that the locomotion and thigmotaxis assays alone cannot capture the complex behaviours that define ASD. As such, more *in vivo* work with both BHB and NMN is required to characterize their effects on additional animal behaviours.

The elucidation of a novel pathway to regulate mitochondrial morphology is an important advancement, given the critical importance of these processes in mediating mitochondrial function, and the increasingly recognized role that mitochondrial dysfunction plays in many disease (Chan, 2020; Whitley et al., 2019). Moreover, restoring the balance between fusion and fission, either by inhibiting fission or by promoting fusion, is beneficial in several neurological disease models. However, there are currently no established direct therapeutic approaches that target mitochondrial fission or fusion in humans. Despite the promise of the KD in this regard, its use may remain somewhat limited due to the risk of undesired side effects and complications. Thus, our findings that BHB and NMN treatments can recapitulate some of the beneficial effects of the KD, have promising therapeutic potential.

Limitations of the study

In the current study, we set out to explore the mechanisms underlying KD-mediated mitochondrial hyperfusion and improvement in ASD behaviours. We identified a mechanistic pathway linking BHB, a key metabolite of the KD, to increased NAD^+ levels and mitochondrial hyperfusion, but there are several limitations to our study. For example, it is important to note that both BHB and NAD^+ have multiple mechanisms of action that likely impact mitochondrial form and function beyond the pathway that we have eluciated. An important future direction would be to investigate the detailed mechanism of how the ketogenic diet (KD) affects NAD+ regulation, including the generation and consumption of NAD+, and the possible involvement of specific enzymes such as iNAMPT, NMNAT1-3, NRK, CD38, and PARPs. In addition, future studies should also explore additional proteins involved in regulating mitochondrial fission and fusion which could also be regulated by acetylation or other mechanisms downstream of BHB and NAD+.

Meanwhile, as we did not obtain robust knockdown of Sirt3, we cannot make definitive conclusions about its role in mediating fusion in response to increased NAD^+. With respect to ASD-related findings, the *shank3*$^{+/-}$ fish model is only one ASD model, and it remains unclear if these findings will extend to other ASD models, let alone to human ASD patients. Furthermore, we have only examined movement behaviours, which do not fully recapitulate the full extent of ASD behaviours, and have only examined one timepoint using a single dose for BHB and NMN. In this regard, testing additional dosing regimens and behaviours would be important to examine in future studies. Finally, it

would also be important to examine the subcellular architecture in the fish model to see if this is altered in *shank3*$^{+/-}$ and rescued by BHB or NMN treatment.

Methods and Materials

Cell Culture: HeLa cells were grown in DMEM, high-glucose media (Cat#11965092, Gibco, USA) containing l-Glutamine and supplemented with 10% fetal bovine serum (FBS). Cells were seeded at 1 x 10^6 cells in 10 cm plates and grown at 37 °C and 5% CO_2 until they were 70-80% confluent (approximately after 48 hrs) before being harvested for analysis or re-seed. At a 50-60% confluency (approximately after 18-24 hrs), cells were treated with BHB (5 mM) (Cat#H6501; Sigma, USA) or NMN (50 µM) (provided by Dr. David Sinclair) or etomoxir (20µM) (Cat#509455; Calbiochem, Sigma, USA) or sirtinol (1mM) (Cat#566321; Calbiochem, Sigma, USA) for 24 hr. In case of experiments where two drugs treated together, both drugs were supplemented in the media together. 24 hr post treatment, cells were harvested by washing with 1x PBS, followed by incubation with 0.25% Trypsin (Corning® Trypsin containing 0.1% EDTA; Fisher Scientific) for 1 min at 37°C and 5% CO_2. Detached cells were collected in fresh media, followed by centrifugation at 5000 RPM for 5 min, and cell pellets were then stored at -20^0C for further experiments. Cells used for immunofluorescence were grown on glass coverslips (no. 1.5 - 12 mm diameter; Electron Microscopy Sciences) that were placed in the same 10cm dishes used for protein analysis.

Immunofluorescence Staining: Cells on coverslips were fixed in 4% paraformaldehyde for 15 min at 37 °C, permeabilized with 0.1% TritonX100, and blocked with 10% FBS in PBS as described previously (Ahn et al., 2020). Mitochondria were labelled with TOMM20 (Cat#186735; Abcam, USA) primary antibodies were used at 1:1000, diluted in 10% FBS in PBS, and cells were incubated overnight at 4 °C. The

appropriate secondary AlexaFluor antibodies were diluted in 10% FBS in PBS at 1:1000, and cells were incubated in the dark at room temperature for 1 hr. Stained cells were then washed in 1X PBS and mounted using Dako mounting media (Cat#S3023, Agilent, USA).

For peroxisome staining, the cells fixed on the coverslips were permeabilized with 0.1% NP-40 dissolved in 1X PBS for 15 minutes at room temperature. This was washed off with PBS and subsequently, 10% FBS was used to block for one hour at room temperature. Following blocking, an overnight incubation was performed to label the peroxisomes with anti-PMP70 (Cat#P0497, Sigma-Aldrich; 1:1000 dilution in blocking solution). The slips were washed three times with PBS before the complementary anti-rabbit secondary antibody was added (Cat#A-11034, Life Technologies; 1:1000 dilution in blocking solution) and incubated for one hour at room temperature. A final washing step with 1X PBS followed and the slips were mounted using the aforementioned mounting media.

Microscopy and Image Morphology Analysis: An Olympus spinning disc confocal system (Olympus SD OSR, Olympus Corporation, Tokyo, Japan) (UAPON 100XOTIRF/1.49 oil objective) operated by Metamorph software was used to image fixed cells. Mitochondrial network morphology was assessed in a blinded fashion and assigned to 3 categories of mitochondrial morphology (fragmented, intermediate, and fused). A representative image under each category is shown in Supplementary Figure 3A. At least 80-150 cells were counted per condition, and the analyses were performed

on 3 independent replicates and 2 independent technical replicates for knockdown study for each treatment condition. Mitochondrial branch length was quantified using the Image-J, MiNA (Valente et al., 2017) plug-in from three independent replicates, using a standard region of interest (ROI) and measured randomly from each image.

For peroxisome analysis of the various treatments, Z-projections were obtained, and images adjusted for threshold, the threshold was set to remove any background signals using Image J. Z projections were generated for average intensity using Image J. The Image J particle analysis tool was used to measure peroxisome size, and counts. For peroxisome size analysis, peroxisomes from 200 cells were analyzed and the sizes binned as follows: elongated (0.2-1) μm^2, intermediate (0.1-0.2) μm^2 or round (0.01-0.1) μm^2. Meanwhile, the mean number of peroxisomes was calculated per cell. Sample size is 88 cells in total, with 2 biological replicates (44 cells/replicate).

Oxygen Consumption: For each well in flat bottom 96 well plate (MaxBioChem), 30,000 HeLa cells were seeded in DMEM culture medium to and allowed to attach overnight. The next day, new media with 5 mM BHB (Cat#H6501; Sigma, USA) or vehicle was added. 24 hours later the oxygen consumption rate (OCR) was measured using the Resipher platform (Lucid Scientific, Atlanta, GA, United States) (Triolo & Khacho, 2024). Real-time continuous OCR measurements were monitored in the incubator. Finally, the OCR was normalized to total protein content estimated using the Pierce™ BCA assay (Cat#A555865; ThermoFisher, USA).

Western blots: Frozen cell lysates were homogenized using RIPA Lysis and Extraction Buffer (Cat#89900, Thermo Fisher, USA) and protease inhibitors cocktail (Cat#10190-060, VWR, USA), on ice for 1hr. Protein content was measured using the Pierce™ BCA Protein Assay Kit (Cat#A555865; ThermoFisher, USA). Depending on the target, 30–40-µg total protein was loaded onto SDS-PAGE for western blotting. Polyvinylidene fluoride (PVDF) membranes were blocked with 5% nonfat milk in Tris-buffered saline solution containing 0.1% Tween 20 (TBS-T) for 1 h. After blocking, the blots were incubated with primary antibody overnight at 4°C. After washing with TBS-T, the blots were incubated with the secondary antibody for 1 h at room temperature. After washing with TBS-T, blots were visualized using an SuperSignal™ West Femto Maximum Sensitivity Substrate (Cat#34095; Fisher Scientific, USA). Bands were detected and quantified using a ChemiDOC MP gel imaging system (Bio-Rad). The following antibodies were used: Actin (Cell Signaling; 1:10,000); DRP1 (BD Biosciences, San Jose, CA, USA; 1:1000); pDRP1^{S616} at (Cell Signaling, Danvers, MA, USA; 1:1000); OPA1 (BD Biosciences; 1:1000); MFN1 (Cat# 3455S, Cell Signaling, USA; 1:1000) ; MFN2 (Cat# M03, Abnova, USA; 1:1000); MFF (Cat#, Cell Signaling, USA; 1:1000); and DRP1 S637 (Cat# 4867SS, Cell Signaling, USA; 1:1000). The expression levels of proteins were normalized to actin for cell lysate, and the ratio of the phosphorylated and total forms was computed using the normalized relative total expression levels. Original blots that were used to crop representative are shown in supplementary figure 6: (A-F)

Immunoprecipitation: Freshly centrifuged cell pallet from the cell lysate collected

after the 24hr treatment (as described in cell culture section) from a 10 cm dish. 250 µl of IP homogenization buffer was used to extract proteins. A custom homogenized buffer was prepared for IP sample homogenization, 150mM NaCL (Cat#BP358212; Fisher Scientific, USA), 50mM Tris-HCL at 7.5 pH (Cat#97063-756; VWR, USA), 5mM EDTA at 8 pH (Cat#E3889; Sigma Adrich, USA), 0.5% NP-40 (Cat#00000; Company), and 1% TritonX (Cat#X100; Sigma Adrich, USA); with freshly added Trichostatin A 1 µM (Cat#A8183; ApexBIO, USA), Nicotinamide 5mM (Cat#N0636; Sigma Adrich, USA), 10mM Sodium Butyrate (Cat#303410; Sigma Adrich, USA) and Protease inhibitor cocktail 1:100 (Cat#M250; Amresco, USA). After 1 hr of incubation, samples were centrifugated at 10000 RPM. Supernatant was diluted accordingly to prepare same amount of protein (350-400ug) and volume (200 µl) followed by protein quantification. Preclearing and washing cell lysate were performed using 20 µl A/G PLUS-Agarose beads per 200 µl sample (Cat#SC2003; Santa Cruz Biotechnology, USA) for 4 hrs followed by centrifugation at 15,000g for 10 minutes at 4^0c. 20 µl of collected supernatant was kept separately to use as input. The leftover supernatant was then incubated with 1.5 µL anti-acetyl-lysine antibody (Cat#9441S; Cell signalling, USA) overnight. 60-70 µl (depending on the protein concentration used in the beginning) A/G PLUS-Agarose beads were added to the antibody incubated samples. Followed by a 4hr rotation and incubation at 4°C, samples were centrifuged at 5,000g for 5 minutes. Supernatant was discarded and the beads pallet was then washed 3 times with the IP homogenization or extraction buffer with all the components. Washing was performed at at 5,000g for 5 minutes each time. Pallets were then heated at 95°C for 5 min with Laemmli buffer (Cat#1610747; Biorad, USA) and centrifuged at 15,000g for 10 minutes

to collect the supernatant. This supernatant was used to perform immunoblotting. Input was prepared checked in a separate gel but same day and setup. Also, a pooled samples (10 µl/sample/group) from all groups ran to show as a positive control, 1 sample input /group was used to run together with IP sample to show the differences. IP sample successfully showed heavy chain and light chain produced due to the A/G bead's reaction. Original blots that were used to crop representative are shown in supplementary figure 8: (A-F)

NAD assay: NAD^+ and NADH were measured as described previously (Zhu & Rand, 2012). Briefly, samples were homogenized in extraction buffer (10 mmol/l Tris/HCl, 0.5% Triton X-100, 10 mmol/l Nicotinamide, pH 7.4) and then centrifuged (12,000 × g for 5 min at 4◦C), after which an aliquot of supernatant was taken for protein quantification. After subsequent extractions with phenol: chloroform: isoamyl alcohol (25:24:1) and chloroform, the supernatant was separated in two aliquots to measure total NAD or NAD+ using a Bio-Rad Imark microplate reader. Data are presented as pmol of NAD^+ or NADH per mg of protein.

siRNA knockdown: TriFECTa RNAi Kits (Integrated DNA Technology, USA) were obtained for SIRT1 (hs.Ri.SIRT1.13), SIRT2 (hs.Ri.SIRT2.13) and Sirt3 (hs.Ri.SIRT3.13). Both a transfection control (TYE563 DsiRNA) (Cat#51-01-20-19), and a negative control DsiRNA (a nontargeting DsiRNA that has no known targets in human, mouse, or rat) (Cat#51-01-14-03), were provided with the kit. 24hrs after siRNA transfection, vehicle, BHB or NMN treatments were initiated, and carried out an

additional 24hr. Lipofectamine™ RNAiMAX (Cat#13778075, Thermo Fisher Scientific, USA) was used as transfection reagent. Cells were platted at $0.5x10^5$ density in a 6 well plate. After 12 hrs of seeding, RNAiMAX (9µl/well) and siRNA (100pmol/well) was diluted in Opti-MEM medium (Cat#31985062, Thermo Fisher Scientific, USA). The mixture of RNAiMAX and siRNA was then added to the well for 24hr. Cells were then collected for western analysis and immunfluorescence to analyse mitochondrial morphology as above.

Zebrafish husbandry, behaviour and genotyping: Zebrafish heterozygous for a *shank3b* mutation (*shank3b*$^{+/-}$) were placed in breeding tanks the afternoon prior to day 0 of the experiment. Males and females were separated by a removable insert, which was removed the morning of the next day to allow breeding. Embryos were consequently collected in petri dishes at a density of ~50 embryos/plate and maintained in E3 medium (60X E3 and methylene blue, diluted in milli Q water) at 28°C. At 10 hours-post fertilization (hpf), zebrafish were either exposed to vehicle (E3 medium), BHB (5 mM), or NMN (50 µM)**.** At 48 hpf, all exposure conditions were washed out thrice and replaced by E3 medium. Zebrafish underwent behavioural assays at 5 days-post fertilization (dpf). Briefly, zebrafish were placed in 48-well plates at a density of 1 fish/well. Locomotion, including distance travelled and speed, was analyzed in each of 15-minutes light and 15-minutes dark via tracking assay using the ZebraBox® recording chamber (Viewpoint Life Sciences, Montreal, QC)**.** Thigmotaxis was measured by comparing the time spent (light conditions) in the inside region of the well versus the perimeter of the well. The thigmotaxis score ranged from -1 to +1 and was calculated

with the following formula: $\boldsymbol{Thigmotaxis\ Score} = \left(\mathbf{2}\left(\frac{s_{inside}}{s_{perimeter}}\right)\right) - \mathbf{1}$. After behavioural assays were completed, zebrafish were genotyped by PCR amplification of the *shank3b* gene with subsequent digestion with T7 endonuclease I (M0302; New England BioLabs). Genotypes were verified on a 2% agarose gel. Mismatched duplexes (seen as three bands on a gel) indicated a heterozygous genotype, whereas single banded samples required further DNA sequencing to indicate a wild type versus homozygous genotype.

Zebrafish oxygen consumption: 2 dpf larval zebrafish were used to measure mitochondrial bioenergetics upon 5 mM BHB exposure from 10 hpf to 2 dpf. Oxygen consumption rates (OCR; pMol/min) and extracellular acidification rates (ECAR; mpH/min) were measured using a XF24 Extracellular Analyzer (Seahorse Biosciences, Billerica, MA). Single zebrafish (n = 7 per treatment group per run) were seeded in an islet microplate, protected by a mesh islet capture screen. To assess zebrafish bioenergetics, we followed a previously published methodology (Stackley et al., 2011). In brief, OCR and ECAR were measured across 27 cycles (2-minutes mixing, 1-minute wait, 2-minute measurement) at basal rates and after exposure to dilutions of 100 µM oligomycin (injected at cycle 7), 37.5 µM carbonyl cyanide p-trifluoro methoxyphenylhydrazone (FCCP; injected at cycle 15), and 30 µM antimycin A (injected at cycle 21). Final measurements were taken as the average of the last 4 cycles for basal respiration, last 3 cycles for oligomycin and antimycin A injections, and last 5 cycles for FCCP injections.

Statistics: Statistical analysis was performed using GraphPad Prism 9 (Version 9.4.1) software (La Jolla, CA, USA). All data are presented as mean ± SEM. Mechanistic data were analyzed using unpaired t-tests to assess significant changes between two groups (e.g., vehicle vs. NMN or vehicle vs. BHB). For the zebrafish assay, data involving multiple factors were analyzed using two-way ANOVA followed by Tukey's post-hoc test. Normality was assessed using the Shapiro-Wilk test for all datasets, and no violations of normality were observed. Significant differences are presented as $*p < 0.05$, $**p < 0.01$, and $**p < 0.001$.

Figure Legends:

Figure 1: BHB and NMN promote mitochondrial elongation and increases NAD^+ in Hela cell. (A) Representative confocal images of HeLa cells stained with antibodies against TOMM20 for mitochondrial network. HeLa cells were immuno-stained after 24h treatment with indicated concentrations of Veh or BHB or NMN or Eto+BHB. **(B)** Quantification of mean mitochondrial branch length were measured between Veh, BHB or NMN or Eto+BHB treated cells. This quantification was performed by Image-J, MiNA plugin from three independent replicates, using a standard region of interest (ROI) and measured randomly from each image. **(C)** Qualitative analysis of mitochondrial morphology was performed in Veh, BHB or NMN or Eto+BHB treated cells via an unbiased visual scoring method. Analysis was done using at least 150 cells per condition, and 3 independent replicates for each treatment condition. **(D)** NAD^+ level was measured 24h post treatment of Veh or BHB or NMN; and Veh or Eto+BHB in HeLa cells (n=3-6/group). Data are shown as mean ± SEM. Data were analyzed using t-test. The significant differences are presented as *** $p < 0.001$.

Figure 2: BHB and NMN acts on mitochondrial fusion and fission machinery and peroxisome differently. (A) Representative blots are presented for the densitometry analysis for **(B)** OPA1 and **(C)** $pDRP^{s616}$ **(D)** total DRP(n=3/group). Separately conducted set of experiments are presented using a dotted line under the same graph. **(E)** Representative confocal images of HeLa cells stained with antibodies against PMP70 for peroxisomes. HeLa cells were immuno-stained after 24h treatment with indicated concentrations of Veh or BHB or Eto+BHB or NMN. **(F)** Quantification of mean number of peroxisomes per cell were measured between Veh, BHB or Eto+BHB or

NMN treated cells. This quantification was performed by Image-J, particle analysis feature, using a standard region of interest (ROI) and measured randomly from all images, with the particle analysis tool. **(G)** Quantitative analysis of sizes of peroxisomes for control and drug treatment(s) and concentration(s) mentioned. Analysis was done using at least 150 cells per condition, and 3 independent replicates for each treatment condition. Data are shown as mean ± SEM. Data were analyzed using t-test. The significant differences are presented as *** $p < 0.001$

Figure 3: BHB and NMN supplementation in HeLa cell reduces acetylation. (A) Representative blots are presented for the densitometry analysis for **(B)** global acetylation in Veh or BHB or NMN treated cells (n=3/group) along with Actin as the loading control; **(C)** acetylated-OPA1 and **(D)** acetylated-DRP1 normalised to input as control (n=3/group). Data are shown as mean ± SEM. Data were analyzed using t-test. The significant differences are presented as *** $p < 0.001$.

Figure 4: Inhibition of Sirtuin 1 and 2, blocks BHB and NMN aided mitochondrial fusion but not the peroxisome network. (A) Representative confocal images of HeLa cells stained with antibodies against TOMM20 for mitochondrial network. HeLa cells were immuno-stained after 24h treatment with indicated concentrations of Veh (Vehicle) or Sirtinol or Sirtinol+BHB or Sirtinol+NMN. **(B)** Quantification of mean mitochondrial branch length and **(C)** Qualitative analysis of mitochondrial morphology were measured between Veh or Sirtinol, Sirtinol+BHB or Sirtinol+NMN treated cells. Analysis was done using at least 150 cells per condition, and 3 independent replicates for each treatment condition. **(D)** Representative confocal images of HeLa cells stained with antibodies against PMP70 for peroxisomes. HeLa cells were immuno-stained after 24h treatment

with indicated concentrations of Veh (Vehicle) or Sirtinol or Sirtinol+BHB or Sirtinol+NMN. **(E)** Quantification of total number of peroxisomes per cell and **(F)** quantitative analysis of peroxisome size(s) were measured between Veh or Sirtinol, Sirtinol+BHB or Sirtinol+NMN treated cells. Analysis was done using at least 150 cells per condition, and 3 independent replicates for each treatment condition. Data are shown as mean ± SEM. Data were analyzed using t-test. The significant differences are presented as *** $p < 0.001$.

Figure 5: BHB promotes mitochondrial fusion via Sirt2 dependent manner. (A) Representative confocal images of HeLa cells stained with antibodies against TOMM20 for mitochondrial network. HeLa cells were immuno-stained 48h post transfection of siRNA targets. 24h post siRNA transfection, with indicated concentrations of BHB or NMN was added for 24h into each siRNA target group. Representative confocal images of HeLa cells stained with antibodies against TOMM20 for mitochondrial network in Sirt1 and Sirt2 KD cells with 24h post treatment of BHB or NMN. Quantification of mean mitochondrial branch length were measured between **(B)** Veh or BHB or NMN. This quantification was performed by Image-J, MiNA plugin from three independent replicates, using a standard region of interest (ROI) and measured randomly from each image. **(C)** Qualitative analysis of mitochondrial morphology was performed in Veh, BHB or NMN treated cells via an unbiased visual scoring method. Analysis was done using at least 80 cells per condition, and 2 technical replicates for each treatment condition. Data are shown as mean ± SEM. Data were analyzed using t-test. The significant differences are presented as *** $p < 0.001$.

Figure 6: BHB and NMN improve movement behaviours in *shank3b+/-* zebrafish. **A)** Exposure and behavioural paradigm where *shank3b*$^{+/+}$ and *shank3b*$^{+/-}$ zebrafish were exposed to vehicle (Veh; E3), BHB (1 mM), or NMN (50 µM) from 10-48 hpf, and movement monitored at 5 dpf. **B)** Representative movement trace. Analysis of distance travelled (mm) in light **(C)** or dark **(D)** conditions. Analysis of average speed (mm/2) in light **(E)** or dark **(F)** conditions. **G)** Thigmotaxis analysis of zebrafish movement comparing time spent in the center or periphery of the well. Data are shown as mean ± SEM. n=14-71 fish. Data were analyzed using two-way ANOVA with post-hoc Tukey test. Relevant significant differences are presented on the figure.

Figure 7: Metabolic effects of BHB and NMN in *shank3+/-* zebrafish. Zebrafish were exposed to vehicle (Veh; E3), BHB (1 mM), or NMN (50 µM) from 10-48 hpf and mitochondrial bioenergetics were measured at 2 dpf. Oxygen consumption rate (OCR; pMol/min) **(A)** and extracellular acidification rate (ECAR; mpH/min) **(B)** were measured basally and following sequential addition of oligomycin, FCCP, and antimycin A as indicated. Data are shown as mean ± SEM. n = 7 per treatment group per run. Data were analyzed using two-way ANOVA with post-hoc Tukey test. Relevant significant differences are presented on the figure.

Authors Contribution: GMU: designed the study, performed experiments, analysed data, coordinated experiments with other collaborators, generated figures, and wrote and edited the manuscript. RL: designed and performed fish behavioural assays (including breeding) and Seahorse assays, analysed data, and contributed to writing and editing. MZ: performed the peroxisome assay and data analysis. AJ: performed cellular oxygen consumption assays IAK: provided technical support for microscopy and siRNA experiments. JMR: obtained funding, designed the study, and edited manuscript. DMK: designed the fish experiments, and edited the manuscript. TES: obtained funding, designed and coordinated the study, and wrote and edited the manuscript as the corresponding author.

Acknowledgements: We thank Dr David A. Sinclair (Professor at the Department of Genetics and Co-Director of the Paul F. Glenn Center for Biology of Aging Research at Harvard Medical School) for kindly providing the NMN.

Ethics Approval: All fish protocols were approved by the University of Calgary Institutional Animal Care and Use Committee, which conform with the Guide for the Care and Use of Laboratory Animals published by the United States National Institutes of Health (eighth edition; revised 2011) and the guidelines of the Canadian Council on Animal Care.

Sources of Funding: This study was supported by funds from the Scottish Rites Charitable Foundation (TES, JMR), and the Alberta Children's Hospital Research

Foundation Neurodevelopment Disorder Program (JMR, TES). MZ was supported by Owerko Center, University of Calgary. GMU was supported by an Alberta Children's Hospital Research Foundation - Cumming School of Medicine postdoctoral fellowship.

Conflict of interest: The authors have declared that no conflict of interest exists

Supplementary Materials:

Supplementary Figure 1: Supplemental Figure 1: Qualitative analyses of mitochondrial network morphology, which are characterized according to the appearance of the mitochondrial network as fused, intermediate, or fragmented, via an unbiased scoring method. Analyses was performed from a total of 150 cells per treatment, with 3 independent replicates for each treatment. Bars indicate mean +/- SD.

Supplementary Figure 2: HeLa cells were pre-treated with BHB or vehicle control for 24 hrs and the basal oxygen consumption rate OCR (fmol/mm^2/s/mg protein) acquired via the Resipher platform. **A)** Basal OCR trace acquired over 10 hrs. Error bars show mean +/- SD. n = 4/group **B)** Basal OCR at 25 hour and 33 hour time points.). Bars show median and points represent replicates. Data were analyzed via unpaired t-test; * $p \leq 0.05$; ** $p \leq 0.01$; *** $p \leq 0.001$; ns, not significant.

Supplementary Figure 3: (A) Representative images for the visual scoring of mitochondrial morphology. **(B)** NAD^+ and **(C)** Total NAD^++NADH level was measured 24h post treatment of Veh or BHB or NMN n HeLa cells. **(D)** Representative blots are presented for the densitometry analysis for mitochondrial fusion and fission related protein expression of **(E)** MFN1, **(F)** MFN2, **(G)** MFF in Veh, and BHB or NMN treated cells (n=3/group). Data are shown as mean ± SEM. Data were analyzed using t-test. The significant differences are presented as *** $p < 0.001$.

Supplementary Figure 4: (A) Representative confocal images of HeLa cells stained with antibodies against TOMM20 for mitochondrial network. HeLa cells were immuno-stained after 24h treatment with indicated concentrations of Veh or BHB or Eto or

Eto+BHB. **(B)** Quantification of mitochondrial average branch length were measured between Veh or BHB or Eto or Eto+BHB treated cells. This quantification was performed by Image-J, MiNA plugin from three independent replicates, using a standard region of interest (ROI) and measured randomly from each image. **(C)** Qualitative analysis of mitochondrial morphology was performed in Veh or BHB or Eto or Eto+BHB treated cells via an unbiased visual scoring method. Analysis was done using at least 150 cells per condition, and 3 independent replicates for each treatment condition. **(D, E)** NAD^+ and total NAD^++NADH level was measured 24h post treatment of Veh, BHB, Eto or Eto+BHB. **(F, G)** Representative blots of global acetylation in Veh, or sirtinol treated cells for 24h (n=3/group) along with Actin as the loading control and their densitometric analysis. **(H, I**) NAD^+ and total NAD^++NADH level was measured 24h post treatment of Veh, Sirtinol, Sirtinol+BHB or Sirtinol+NMN in HeLa cells respectively. Data are shown as mean ± SEM. Data were analyzed using t-test. The significant differences are presented as *** $p < 0.001$.

Supplementary Figure 5: (A) Representative confocal images of HeLa cells stained with antibodies against TOMM20 for mitochondrial network. **(A)** The HeLa cells were immuno-stained 48h post transfection of siSirt1 (target1, target 2 and target 3). 24h post siRNA transfection, with indicated concentrations of BHB or NMN was added for 24h into each siRNA target group. **(B)** Quantification of mitochondrial average branch length were measured between the indicated groups in each siRNA targets. This quantification was performed by Image-J, MiNA plugin from three independent replicates, using a standard region of interest (ROI) and measured randomly from each image. **(C)** Qualitative quantification of mitochondrial morphology was performed between the

indicated groups in each siRNA targets via an unbiased visual scoring method. Analysis was done using at least 80 cells per condition, and 2 technical replicates for each treatment condition. Data are shown as mean ± SEM. Data were analyzed using t-test. The significant differences are presented as *** $p < 0.001$.

Supplementary Figure 6: (A) Representative confocal images of HeLa cells stained with antibodies against TOMM20 for mitochondrial network. **(A)** The HeLa cells were immuno-stained 48h post transfection of siSirt2 (target1, target 2 and target 3). 24h post siRNA transfection, with indicated concentrations of BHB or NMN was added for 24h into each siRNA target group. **(B)** Quantification of mitochondrial average branch length were measured between the indicated groups in each siRNA targets. This quantification was performed by Image-J, MiNA plugin from three independent replicates, using a standard region of interest (ROI) and measured randomly from each image. **(C)** Qualitative quantification of mitochondrial morphology was performed between the indicated groups in each siRNA targets via an unbiased visual scoring method. Analysis was done using at least 80 cells per condition, and 2 technical replicates for each treatment condition. Data are shown as mean ± SEM. Data were analyzed using t-test. The significant differences are presented as *** $p < 0.001$.

Supplementary Figure 7: (A) Representative confocal images of HeLa cells stained with antibodies against TOMM20 for mitochondrial network. **(A)** The HeLa cells were immuno-stained 48h post transfection of siSirt3 (target1, target 2 and target 3). 24h post siRNA transfection, with indicated concentrations of BHB or NMN was added for 24h into each siRNA target group. **(B)** Quantification of mitochondrial average branch length were measured between the indicated groups in each siRNA targets. This quantification

was performed by Image-J, MiNA plugin from three independent replicates, using a standard region of interest (ROI) and measured randomly from each image. **(C)** Qualitative quantification of mitochondrial morphology was performed between the indicated groups in each siRNA targets via an unbiased visual scoring method. Analysis was done using at least 80 cells per condition, and 2 technical replicates for each treatment condition. Data are shown as mean ± SEM. Data were analyzed using t-test. The significant differences are presented as *** $p < 0.001$.

Supplementary Figure 8: (A-F) Original blots presented that was used to present the representative bands in analysis and figures.

References

Ahn, Sabouny, R., Villa, B. R., Yee, N. C., Mychasiuk, R., Uddin, G. M.,…Shutt, T. E. (2020). Aberrant Mitochondrial Morphology and Function in the BTBR Mouse Model of Autism Is Improved by Two Weeks of Ketogenic Diet. *Int J Mol Sci*, *21*(9). https://doi.org/10.3390/ijms21093266

Ahn, Y., Narous, M., Tobias, R., Rho, J. M., & Mychasiuk, R. (2014). The ketogenic diet modifies social and metabolic alterations identified in the prenatal valproic acid model of autism spectrum disorder. *Dev Neurosci*, *36*(5), 371-380. https://doi.org/10.1159/000362645

Ahn, Y., Sabouny, R., Villa, B. R., Yee, N. C., Mychasiuk, R., Uddin, G. M.,…Shutt, T. E. (2020). Aberrant mitochondrial morphology and function in the BTBR mouse model of autism is improved by two weeks of ketogenic diet. *International journal of molecular sciences*, *21*(9), 3266.

Baker, N., Patel, J., & Khacho, M. (2019). Linking mitochondrial dynamics, cristae remodeling and supercomplex formation: how mitochondrial structure can regulate bioenergetics. *Mitochondrion*, *49*, 259-268.

Barone, R., Bastin, J., Djouadi, F., Singh, I., Karim, M. A., Ammanamanchi, A.,…Frye, R. E. (2021). Mitochondrial Fatty Acid beta-Oxidation and Resveratrol Effect in Fibroblasts from Patients with Autism Spectrum Disorder. *J Pers Med*, *11*(6). https://doi.org/10.3390/jpm11060510

Biel, T. G., Lee, S., Flores-Toro, J. A., Dean, J. W., Go, K. L., Lee, M. H.,…Kim, J. S. (2016). Sirtuin 1 suppresses mitochondrial dysfunction of ischemic mouse livers in a mitofusin 2-dependent manner. *Cell Death Differ*, *23*(2), 279-290. https://doi.org/10.1038/cdd.2015.96

Bonkowski, M. S., & Sinclair, D. A. (2016). Slowing ageing by design: the rise of NAD(+) and sirtuin-activating compounds. *Nat Rev Mol Cell Biol*, *17*(11), 679-690. https://doi.org/10.1038/nrm.2016.93

Chan, D. C. (2020). Mitochondrial dynamics and its involvement in disease. *Annual review of pathology: mechanisms of disease*, *15*, 235-259.

Citrigno, L., Muglia, M., Qualtieri, A., Spadafora, P., Cavalcanti, F., Pioggia, G., & Cerasa, A. (2020). The Mitochondrial Dysfunction Hypothesis in Autism Spectrum Disorders: Current Status and Future Perspectives. *Int J Mol Sci*, *21*(16). https://doi.org/10.3390/ijms21165785

Covarrubias, A. J., Perrone, R., Grozio, A., & Verdin, E. (2021). NAD(+) metabolism and its roles in cellular processes during ageing. *Nat Rev Mol Cell Biol*, *22*(2), 119-141. https://doi.org/10.1038/s41580-020-00313-x

Dreyer, C., Keller, H., Mahfoudi, A., Laudet, V., Krey, G., & Wahli, W. (1993). Positive regulation of the peroxisomal beta-oxidation pathway by fatty acids through activation of peroxisome proliferator-activated receptors (PPAR). *Biol Cell*, *77*(1), 67-76. https://doi.org/10.1016/s0248-4900(05)80176-5

Durand, C. M., Betancur, C., Boeckers, T. M., Bockmann, J., Chaste, P., Fauchereau, F.,…Bourgeron, T. (2007). Mutations in the gene encoding the synaptic scaffolding protein SHANK3 are associated with autism spectrum disorders. *Nat Genet*, *39*(1), 25-27. https://doi.org/10.1038/ng1933

848 El-Rashidy, O., El-Baz, F., El-Gendy, Y., Khalaf, R., Reda, D., & Saad, K. (2017). Ketogenic diet
849 versus gluten free casein free diet in autistic children: a case-control study. *Metab Brain*
850 *Dis*, *32*(6), 1935-1941. https://doi.org/10.1007/s11011-017-0088-z
851 Elamin, M., Ruskin, D. N., Masino, S. A., & Sacchetti, P. (2017). Ketone-Based Metabolic
852 Therapy: Is Increased NAD(+) a Primary Mechanism? *Front Mol Neurosci*, *10*, 377.
853 https://doi.org/10.3389/fnmol.2017.00377
854 Evangeliou, A., Vlachonikolis, I., Mihailidou, H., Spilioti, M., Skarpalezou, A., Makaronas,
855 N.,…Smeitink, J. (2003). Application of a ketogenic diet in children with autistic behavior:
856 pilot study. *J Child Neurol*, *18*(2), 113-118.
857 https://doi.org/10.1177/08830738030180020501
858 Fang, E. F., Hou, Y., Palikaras, K., Adriaanse, B. A., Kerr, J. S., Yang, B.,…Bohr, V. A. (2019).
859 Mitophagy inhibits amyloid-β and tau pathology and reverses cognitive deficits in
860 models of Alzheimer's disease. *Nat Neurosci*, *22*(3), 401-412.
861 https://doi.org/10.1038/s41593-018-0332-9
862 Fang, E. F., Scheibye-Knudsen, M., Brace, L. E., Kassahun, H., SenGupta, T., Nilsen, H.,…Bohr, V.
863 A. (2014). Defective mitophagy in XPA via PARP-1 hyperactivation and NAD(+)/SIRT1
864 reduction. *Cell*, *157*(4), 882-896. https://doi.org/10.1016/j.cell.2014.03.026
865 Frye, R. E., Lionnard, L., Singh, I., Karim, M. A., Chajra, H., Frechet, M.,…Aouacheria, A. (2021).
866 Mitochondrial morphology is associated with respiratory chain uncoupling in autism
867 spectrum disorder. *Transl Psychiatry*, *11*(1), 527. https://doi.org/10.1038/s41398-021-
868 01647-6
869 Galmozzi, A., Mitro, N., Ferrari, A., Gers, E., Gilardi, F., Godio, C.,…Crestani, M. (2013). Inhibition
870 of class I histone deacetylases unveils a mitochondrial signature and enhances oxidative
871 metabolism in skeletal muscle and adipose tissue. *Diabetes*, *62*(3), 732-742.
872 https://doi.org/10.2337/db12-0548
873 Gevezova, M., Minchev, D., Pacheva, I., Sbirkov, Y., Yordanova, R., Timova, E.,…Sarafian, V.
874 (2021). Cellular Bioenergetic and Metabolic Changes in Patients with Autism Spectrum
875 Disorder. *Curr Top Med Chem*, *21*(11), 985-994.
876 https://doi.org/10.2174/1568026621666210521142131
877 Gilmour, B. C., Gudmundsrud, R., Frank, J., Hov, A., Lautrup, S., Aman, Y.,…Fang, E. F. (2020).
878 Targeting NAD(+) in translational research to relieve diseases and conditions of
879 metabolic stress and ageing. *Mech Ageing Dev*, *186*, 111208.
880 https://doi.org/10.1016/j.mad.2020.111208
881 Glancy, B., Kim, Y., Katti, P., & Willingham, T. B. (2020). The functional impact of mitochondrial
882 structure across subcellular scales. *Frontiers in physiology*, *11*.
883 Gogou, M., & Kolios, G. (2018). Are therapeutic diets an emerging additional choice in autism
884 spectrum disorder management? *World J Pediatr*, *14*(3), 215-223.
885 https://doi.org/10.1007/s12519-018-0164-4
886 Hess, R., Staubli, W., & Riess, W. (1965). Nature of the hepatomegalic effect produced by ethyl-
887 chlorophenoxy-isobutyrate in the rat. *Nature*, *208*(5013), 856-858.
888 https://doi.org/10.1038/208856a0
889 Hu, Q., Zhang, H., Gutierrez Cortes, N., Wu, D., Wang, P., Zhang, J.,…Wang, W. (2020). Increased
890 Drp1 Acetylation by Lipid Overload Induces Cardiomyocyte Death and Heart

891 Dysfunction. *Circ Res*, *126*(4), 456-470.
892 https://doi.org/10.1161/CIRCRESAHA.119.315252
893 Ibhazehiebo K., Gavrilovici C., de la Hoz C.L., Ma S.C., Rehak R., Kaushik G., Meza Santoscoy P.L.,
894 Scott L., Nath N., Kim D.Y., Rho J.M., Kurrasch D.M. (2018). A novel metabolism-based
895 phenotypic drug discovery platform in zebrafish uncovers HDACs 1 and 3 as a potential
896 combined anti-seizure drug target. *Brain*. https://doi.org/10.1093/brain/awx364
897 Ilieva, M., Aldana, B. I., Vinten, K. T., Hohmann, S., Woofenden, T. W., Lukjanska, R.,…Michel, T.
898 M. (2022). Proteomic phenotype of cerebral organoids derived from autism spectrum
899 disorder patients reveal disrupted energy metabolism, cellular components, and
900 biological processes. *Mol Psychiatry*. https://doi.org/10.1038/s41380-022-01627-2
901 Kalueff, A. V., Stewart, A. M., & Gerlai, R. (2014). Zebrafish as an emerging model for studying
902 complex brain disorders. *Trends Pharmacol Sci*, *35*(2), 63-75.
903 https://doi.org/10.1016/j.tips.2013.12.002
904 Kang, H. C., Chung, D. E., Kim, D. W., & Kim, H. D. (2004). Early- and late-onset complications of
905 the ketogenic diet for intractable epilepsy. *Epilepsia*, *45*(9), 1116-1123.
906 https://doi.org/10.1111/j.0013-9580.2004.10004.x
907 Kartawy, M., Khaliulin, I., & Amal, H. (2021). Systems Biology Reveals S-Nitrosylation-Dependent
908 Regulation of Mitochondrial Functions in Mice with Shank3 Mutation Associated with
909 Autism Spectrum Disorder. *Brain Sci*, *11*(6). https://doi.org/10.3390/brainsci11060677
910 Kashiwaya, Y., Takeshima, T., Mori, N., Nakashima, K., Clarke, K., & Veech, R. L. (2000). D-beta-
911 hydroxybutyrate protects neurons in models of Alzheimer's and Parkinson's disease.
912 *Proc Natl Acad Sci U S A*, *97*(10), 5440-5444. https://doi.org/10.1073/pnas.97.10.5440
913 Klimova, N., Long, A., & Kristian, T. (2019). Nicotinamide mononucleotide alters mitochondrial
914 dynamics by SIRT3-dependent mechanism in male mice. *J Neurosci Res*, *97*(8), 975-990.
915 https://doi.org/10.1002/jnr.24397
916 Lee, Kapur, M., Li, M., Choi, M. C., Choi, S., Kim, H. J.,…Yao, T. P. (2014). MFN1 deacetylation
917 activates adaptive mitochondrial fusion and protects metabolically challenged
918 mitochondria. *J Cell Sci*, *127*(Pt 22), 4954-4963. https://doi.org/10.1242/jcs.157321
919 Lee, R. W. Y., Corley, M. J., Pang, A., Arakaki, G., Abbott, L., Nishimoto, M.,…Wong, M. (2018). A
920 modified ketogenic gluten-free diet with MCT improves behavior in children with autism
921 spectrum disorder. *Physiol Behav*, *188*, 205-211.
922 https://doi.org/10.1016/j.physbeh.2018.02.006
923 Lee, S., Chun, H. S., Lee, J., Park, H. J., Kim, K. T., Kim, C. H.,…Kim, W. K. (2018). Plausibility of the
924 zebrafish embryos/larvae as an alternative animal model for autism: A comparison study
925 of transcriptome changes. *PLoS One*, *13*(9), e0203543.
926 https://doi.org/10.1371/journal.pone.0203543
927 Lee, Y., Ryu, J. R., Kang, H., Kim, Y., Kim, S., Zhang, Y.,…Han, K. (2017). Characterization of the
928 zinc-induced Shank3 interactome of mouse synaptosome. *Biochem Biophys Res*
929 *Commun*, *494*(3-4), 581-586. https://doi.org/10.1016/j.bbrc.2017.10.143
930 Lin, A., Turner, Z., Doerrer, S. C., Stanfield, A., & Kossoff, E. H. (2017). Complications During
931 Ketogenic Diet Initiation: Prevalence, Treatment, and Influence on Seizure Outcomes.
932 *Pediatr Neurol*, *68*, 35-39. https://doi.org/10.1016/j.pediatrneurol.2017.01.007

933 Liu, C. X., Li, C. Y., Hu, C. C., Wang, Y., Lin, J., Jiang, Y. H.,…Xu, X. (2018). CRISPR/Cas9-induced
934 shank3b mutant zebrafish display autism-like behaviors. *Mol Autism*, *9*, 23.
935 https://doi.org/10.1186/s13229-018-0204-x
936 Lopaschuk, G. D., Karwi, Q. G., Ho, K. L., Pherwani, S., & Ketema, E. B. (2020). Ketone
937 metabolism in the failing heart. *Biochim Biophys Acta Mol Cell Biol Lipids*, *1865*(12),
938 158813. https://doi.org/10.1016/j.bbalip.2020.158813
939 Mai, A., Massa, S., Lavu, S., Pezzi, R., Simeoni, S., Ragno, R.,…Sinclair, D. A. (2005). Design,
940 synthesis, and biological evaluation of sirtinol analogues as class III histone/protein
941 deacetylase (Sirtuin) inhibitors. *J Med Chem*, *48*(24), 7789-7795.
942 https://doi.org/10.1021/jm050100l
943 Miyamoto, J., Ohue-Kitano, R., Mukouyama, H., Nishida, A., Watanabe, K., Igarashi,
944 M.,…Kimura, I. (2019). Ketone body receptor GPR43 regulates lipid metabolism under
945 ketogenic conditions. *Proc Natl Acad Sci U S A*, *116*(47), 23813-23821.
946 https://doi.org/10.1073/pnas.1912573116
947 Monteiro, P., & Feng, G. (2017). SHANK proteins: roles at the synapse and in autism spectrum
948 disorder. *Nat Rev Neurosci*, *18*(3), 147-157. https://doi.org/10.1038/nrn.2016.183
949 Napoli, E., Duenas, N., & Giulivi, C. (2014). Potential therapeutic use of the ketogenic diet in
950 autism spectrum disorders. *Front Pediatr*, *2*, 69.
951 https://doi.org/10.3389/fped.2014.00069
952 Neal, E. G., Chaffe, H., Schwartz, R. H., Lawson, M. S., Edwards, N., Fitzsimmons, G.,…Cross, J. H.
953 (2008). The ketogenic diet for the treatment of childhood epilepsy: a randomised
954 controlled trial. *Lancet Neurol*, *7*(6), 500-506. https://doi.org/10.1016/S1474-
955 4422(08)70092-9
956 Newman, J. C., & Verdin, E. (2014). beta-hydroxybutyrate: much more than a metabolite.
957 *Diabetes Res Clin Pract*, *106*(2), 173-181. https://doi.org/10.1016/j.diabres.2014.08.009
958 Newman, J. C., & Verdin, E. (2017). beta-Hydroxybutyrate: A Signaling Metabolite. *Annu Rev*
959 *Nutr*, *37*, 51-76. https://doi.org/10.1146/annurev-nutr-071816-064916
960 Oanh, N. T. K., Park, Y. Y., & Cho, H. (2017). Mitochondria elongation is mediated through SIRT1-
961 mediated MFN1 stabilization. *Cell Signal*, *38*, 67-75.
962 https://doi.org/10.1016/j.cellsig.2017.06.019
963 Pecorelli, A., Ferrara, F., Messano, N., Cordone, V., Schiavone, M. L., Cervellati, F.,…Valacchi, G.
964 (2020). Alterations of mitochondrial bioenergetics, dynamics, and morphology support
965 the theory of oxidative damage involvement in autism spectrum disorder. *FASEB J*,
966 *34*(5), 6521-6538. https://doi.org/10.1096/fj.201902677R
967 Rossignol, D. A., & Frye, R. E. (2012). Mitochondrial dysfunction in autism spectrum disorders: a
968 systematic review and meta-analysis. *Mol Psychiatry*, *17*(3), 290-314.
969 https://doi.org/10.1038/mp.2010.136
970 Ruskin, D. N., Murphy, M. I., Slade, S. L., & Masino, S. A. (2017). Ketogenic diet improves
971 behaviors in a maternal immune activation model of autism spectrum disorder. *PLoS*
972 *One*, *12*(2), e0171643. https://doi.org/10.1371/journal.pone.0171643
973 Ruskin, D. N., Svedova, J., Cote, J. L., Sandau, U., Rho, J. M., Kawamura, M., Jr.,…Masino, S. A.
974 (2013). Ketogenic diet improves core symptoms of autism in BTBR mice. *PLoS One*, *8*(6),
975 e65021. https://doi.org/10.1371/journal.pone.0065021

976 Sabouny, R., & Shutt, T. E. (2020). Reciprocal Regulation of Mitochondrial Fission and Fusion.
977 *Trends Biochem Sci*, *45*(7), 564-577. https://doi.org/10.1016/j.tibs.2020.03.009
978 Samant, S. A., Zhang, H. J., Hong, Z., Pillai, V. B., Sundaresan, N. R., Wolfgeher, D.,…Gupta, M. P.
979 (2014). SIRT3 deacetylates and activates OPA1 to regulate mitochondrial dynamics
980 during stress. *Mol Cell Biol*, *34*(5), 807-819. https://doi.org/10.1128/MCB.01483-13
981 Santra, S., Gilkerson, R. W., Davidson, M., & Schon, E. A. (2004). Ketogenic treatment reduces
982 deleted mitochondrial DNAs in cultured human cells. *Ann Neurol*, *56*(5), 662-669.
983 https://doi.org/10.1002/ana.20240
984 Scheibye-Knudsen, M., Mitchell, S. J., Fang, E. F., Iyama, T., Ward, T., Wang, J.,…Bohr, V. A.
985 (2014). A high-fat diet and NAD(+) activate Sirt1 to rescue premature aging in cockayne
986 syndrome. *Cell Metab*, *20*(5), 840-855. https://doi.org/10.1016/j.cmet.2014.10.005
987 Sheng, X., & Cristea, I. M. (2021). The antiviral sirtuin 3 bridges protein acetylation to
988 mitochondrial integrity and metabolism during human cytomegalovirus infection. *PLoS*
989 *Pathog*, *17*(4), e1009506. https://doi.org/10.1371/journal.ppat.1009506
990 Shimazu, T., Hirschey, M. D., Newman, J., He, W., Shirakawa, K., Le Moan, N.,…Verdin, E. (2013).
991 Suppression of oxidative stress by beta-hydroxybutyrate, an endogenous histone
992 deacetylase inhibitor. *Science*, *339*(6116), 211-214.
993 https://doi.org/10.1126/science.1227166
994 Shutt, T. E., & McBride, H. M. (2013). Staying cool in difficult times: mitochondrial dynamics,
995 quality control and the stress response. *Biochim Biophys Acta*, *1833*(2), 417-424.
996 https://doi.org/10.1016/j.bbamcr.2012.05.024
997 Singh, K., Singh, I. N., Diggins, E., Connors, S. L., Karim, M. A., Lee, D.,…Frye, R. E. (2020).
998 Developmental regression and mitochondrial function in children with autism. *Ann Clin*
999 *Transl Neurol*, *7*(5), 683-694. https://doi.org/10.1002/acn3.51034
1000 Spilioti, M., Evangeliou, A. E., Tramma, D., Theodoridou, Z., Metaxas, S., Michailidi, E.,…Gibson,
1001 K. M. (2013). Evidence for treatable inborn errors of metabolism in a cohort of 187
1002 Greek patients with autism spectrum disorder (ASD). *Front Hum Neurosci*, *7*, 858.
1003 https://doi.org/10.3389/fnhum.2013.00858
1004 Stackley, K. D., Beeson, C. C., Rahn, J. J., & Chan, S. S. L. (2011). Bioenergetic Profiling of
1005 Zebrafish
1006 Embryonic Development. *PLOS ONE*, *6*(9), e25652.
1007 https://doi.org/10.1371/journal.pone.0025652
1008 Tang, G., Gutierrez Rios, P., Kuo, S. H., Akman, H. O., Rosoklija, G., Tanji, K.,…Sulzer, D. (2013).
1009 Mitochondrial abnormalities in temporal lobe of autistic brain. *Neurobiol Dis*, *54*, 349-
1010 361. https://doi.org/10.1016/j.nbd.2013.01.006
1011 Thorsen, M. (2020). Oxidative stress, metabolic and mitochondrial abnormalities associated
1012 with autism spectrum disorder. *Prog Mol Biol Transl Sci*, *173*, 331-354.
1013 https://doi.org/10.1016/bs.pmbts.2020.04.018
1014 Triolo, M., & Khacho, M. (2024). Protocol to monitor live-cell, real-time, mitochondrial
1015 respiration in mouse muscle cells using the Resipher platform. *STAR Protocols*, 5(4),
1016 103330. https://doi.org/10.1016/j.xpro.2024.103330
1017 Uddin, G. M., Abbas, R., & Shutt, T. E. (2021). The role of protein acetylation in regulating
1018 mitochondrial fusion and fission. *Biochem Soc Trans*, *49*(6), 2807-2819.
1019 https://doi.org/10.1042/BST20210798

1020 Valente, A. J., Maddalena, L. A., Robb, E. L., Moradi, F., & Stuart, J. A. (2017). A simple ImageJ
1021 macro tool for analyzing mitochondrial network morphology in mammalian cell culture.
1022 *Acta Histochem*, *119*(3), 315-326. https://doi.org/10.1016/j.acthis.2017.03.001
1023 Wai, T., & Langer, T. (2016). Mitochondrial Dynamics and Metabolic Regulation. *Trends*
1024 *Endocrinol Metab*, *27*(2), 105-117. https://doi.org/10.1016/j.tem.2015.12.001
1025 Weber, D. D., Aminzadeh-Gohari, S., Tulipan, J., Catalano, L., Feichtinger, R. G., & Kofler, B.
1026 (2020). Ketogenic diet in the treatment of cancer - Where do we stand? *Mol Metab*, *33*,
1027 102-121. https://doi.org/10.1016/j.molmet.2019.06.026
1028 Weissman, J. R., Kelley, R. I., Bauman, M. L., Cohen, B. H., Murray, K. F., Mitchell, R.
1029 L.,…Natowicz, M. R. (2008). Mitochondrial disease in autism spectrum disorder patients:
1030 a cohort analysis. *PLoS One*, *3*(11), e3815.
1031 https://doi.org/10.1371/journal.pone.0003815
1032 Whitley, B. N., Engelhart, E. A., & Hoppins, S. (2019). Mitochondrial dynamics and their
1033 potential as a therapeutic target. *Mitochondrion*, *49*, 269-283.
1034 https://doi.org/10.1016/j.mito.2019.06.002
1035 Xu, F. Y., Taylor, W. A., Hurd, J. A., & Hatch, G. M. (2003). Etomoxir mediates differential
1036 metabolic channeling of fatty acid and glycerol precursors into cardiolipin in H9c2 cells. *J*
1037 *Lipid Res*, *44*(2), 415-423. https://doi.org/10.1194/jlr.M200335-JLR200
1038 Yang, H., Sibilla, C., Liu, R., Yun, J., Hay, B. A., Blackstone, C.,…Guo, M. (2022). Clueless/CLUH
1039 regulates mitochondrial fission by promoting recruitment of Drp1 to mitochondria. *Nat*
1040 *Commun*, *13*(1), 1582. https://doi.org/10.1038/s41467-022-29071-4
1041 Zhao, Z., Lange, D. J., Voustianiouk, A., MacGrogan, D., Ho, L., Suh, J.,…Pasinetti, G. M. (2006). A
1042 ketogenic diet as a potential novel therapeutic intervention in amyotrophic lateral
1043 sclerosis. *BMC Neurosci*, *7*, 29. https://doi.org/10.1186/1471-2202-7-29
1044 Zhu, C. T., & Rand, D. M. (2012). A hydrazine coupled cycling assay validates the decrease in
1045 redox ratio under starvation in Drosophila. *PLoS One*, *7*(10), e47584.
1046 https://doi.org/10.1371/journal.pone.0047584

1047

Figure 1

A

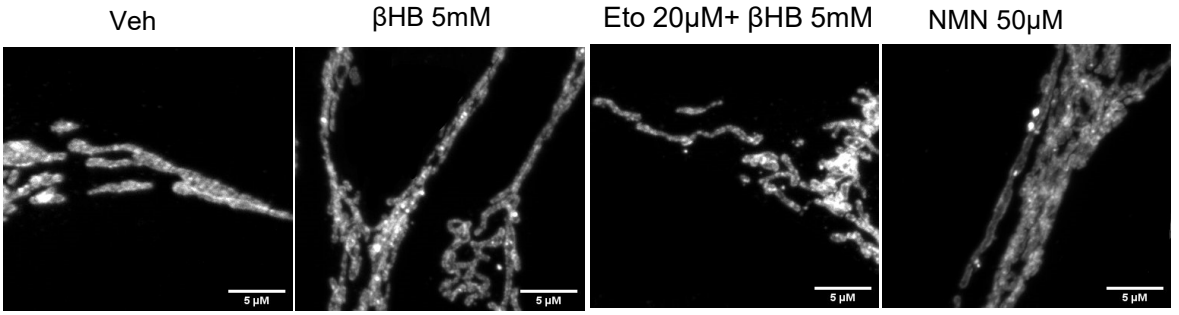

B

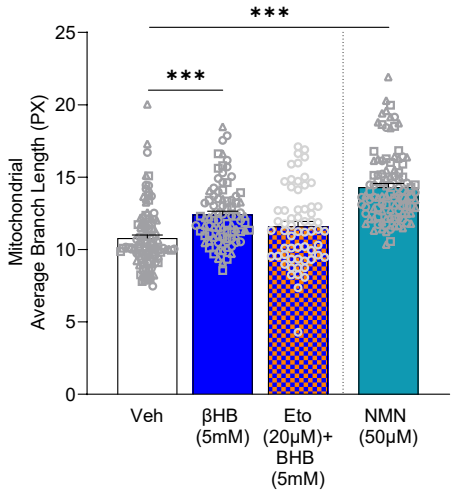

C

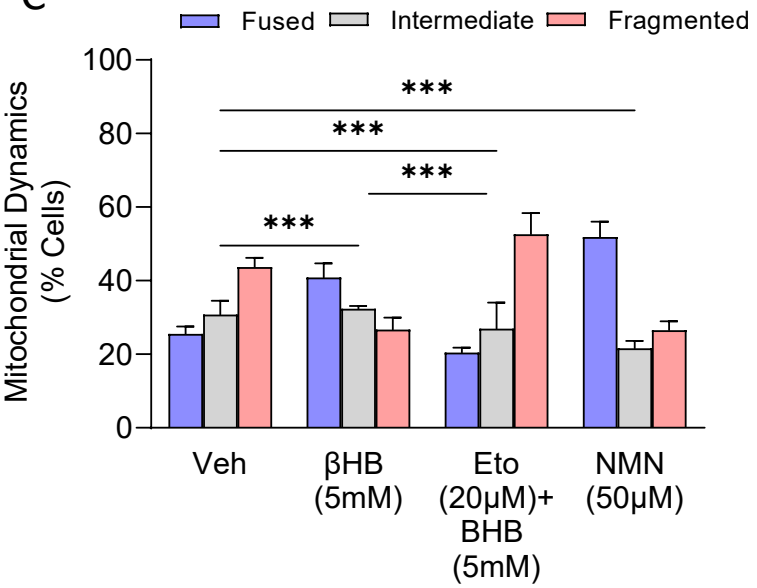

D

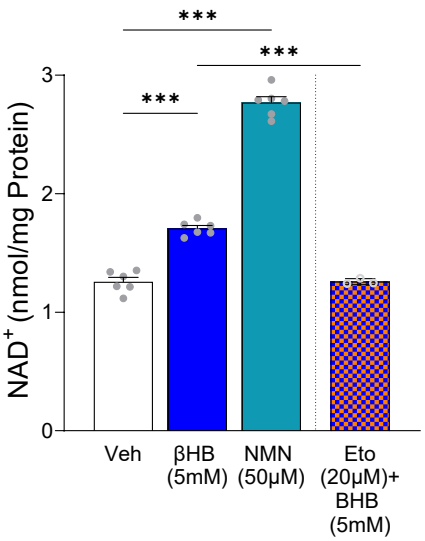

Figure 2

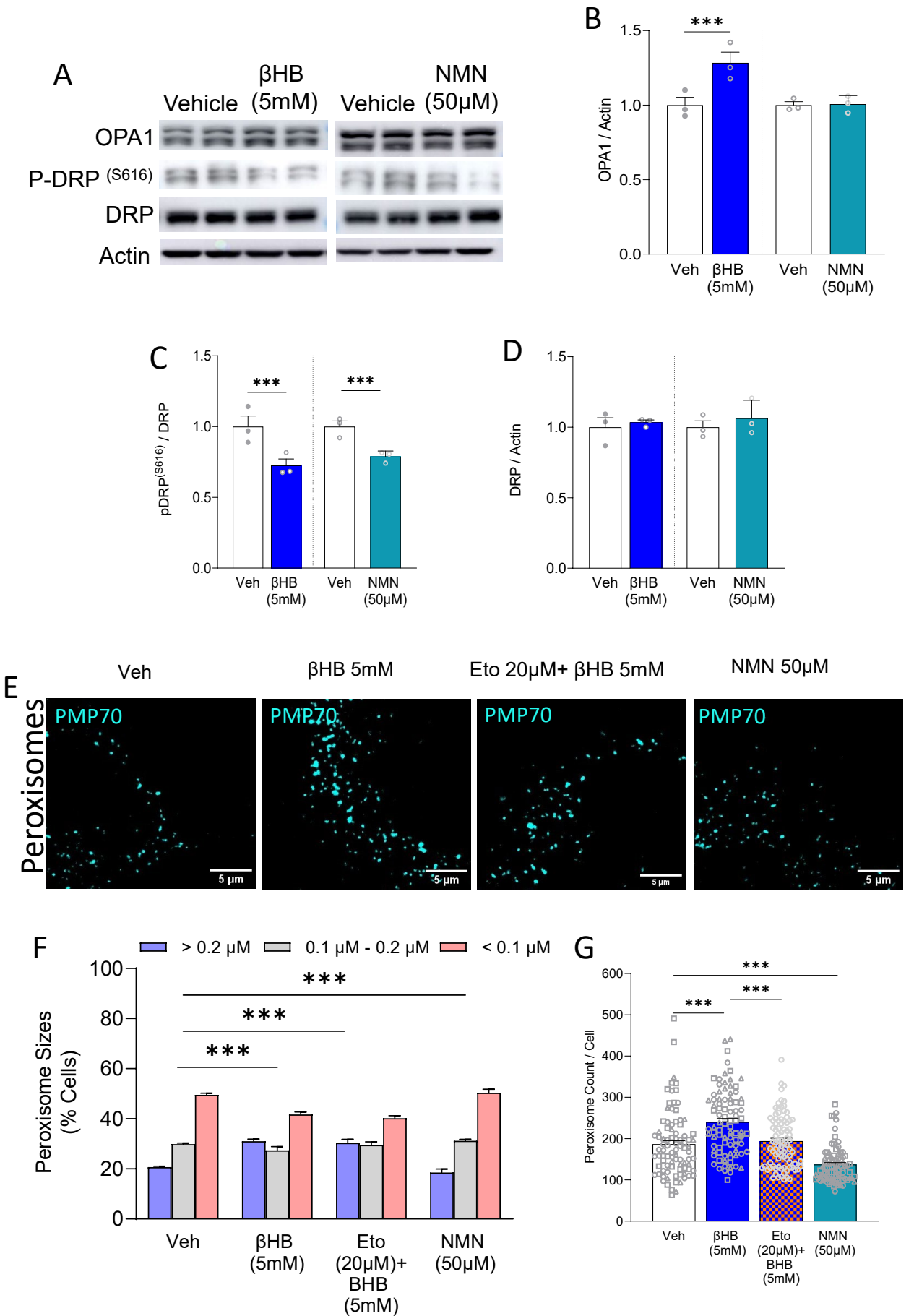
A
Vehicle
βHB (5mM)
Vehicle
NMN (50μM)
OPA1
P-DRP (S616)
DRP
Actin
B
OPA1 / Actin
***
Veh
βHB (5mM)
Veh
NMN (50μM)
C
pDRP(S616) / DRP
***
***
D
DRP / Actin
E
Veh
βHB 5mM
Eto 20μM+ βHB 5mM
NMN 50μM
Peroxisomes
PMP70
5 μm
F
> 0.2 μM
0.1 μM - 0.2 μM
< 0.1 μM
Peroxisome Sizes (% Cells)
***
Veh
βHB (5mM)
Eto (20μM)+ BHB (5mM)
NMN (50μM)
G
Peroxisome Count / Cell

Figure 3

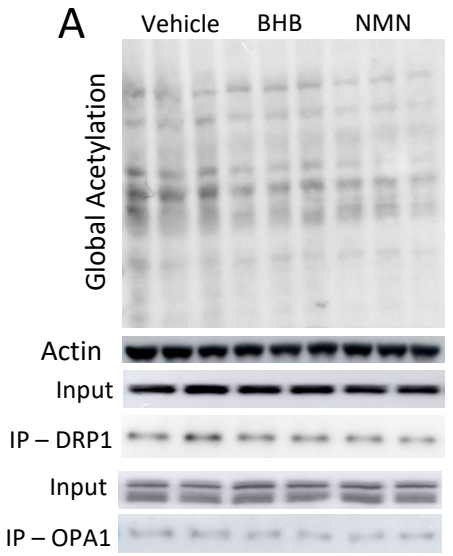
A
Vehicle
BHB
NMN
Global Acetylation
Actin
Input
IP – DRP1
Input
IP – OPA1

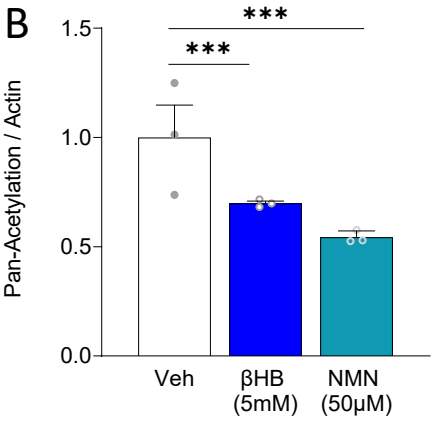
B
Pan-Acetylation / Actin
1.5
1.0
0.5
0.0
***
***
Veh
βHB (5mM)
NMN (50μM)

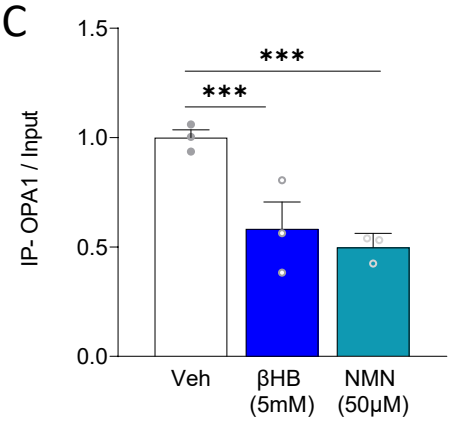
C
IP- OPA1 / Input
1.5
1.0
0.5
0.0
***
***
Veh
βHB (5mM)
NMN (50μM)

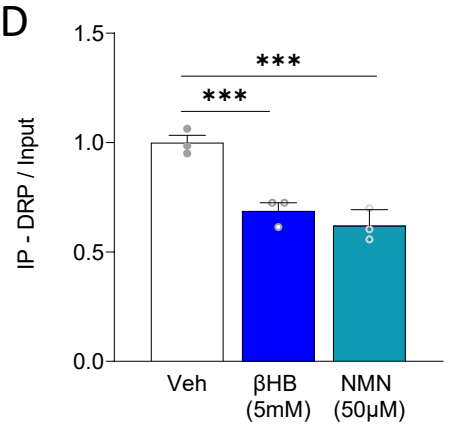
D
IP - DRP / Input
1.5
1.0
0.5
0.0
***
***
Veh
βHB (5mM)
NMN (50μM)

Figure 4

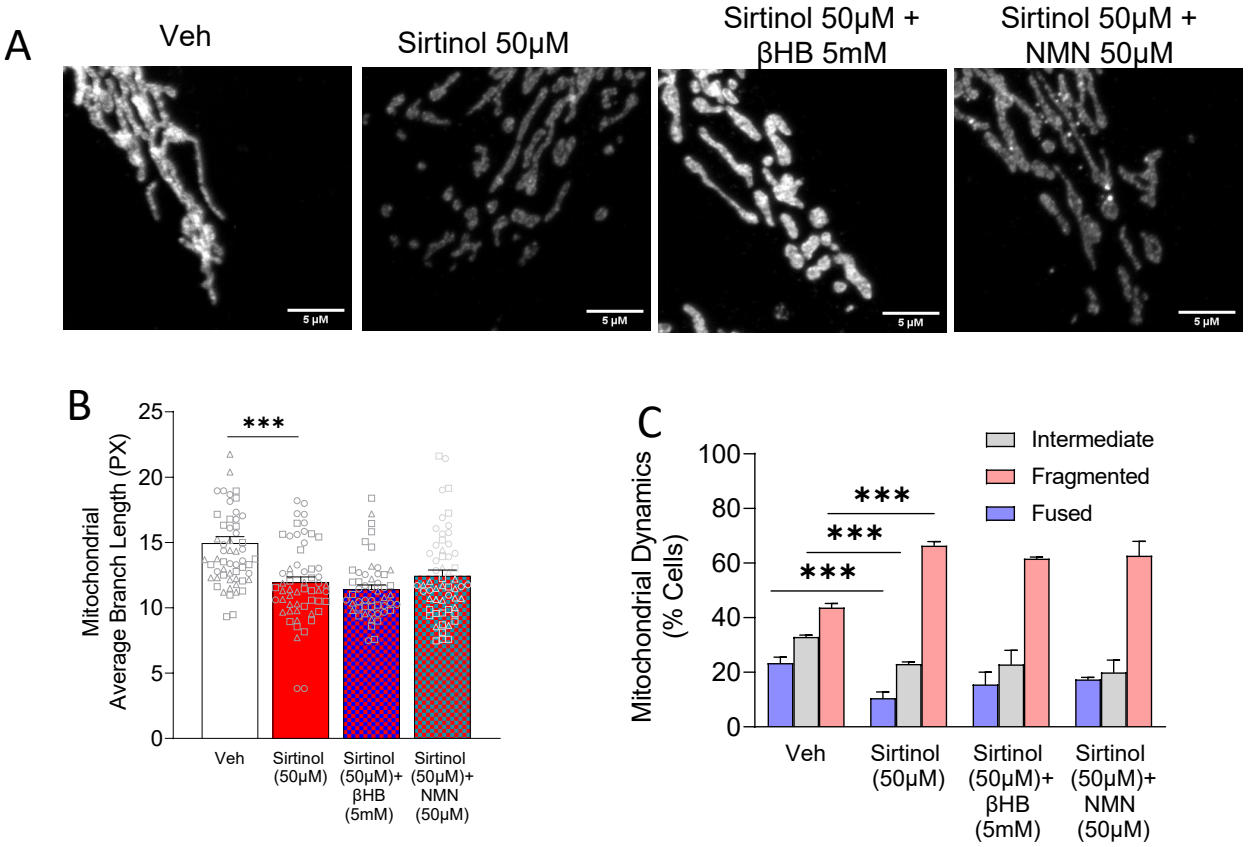
A
Veh
Sirtinol 50μM
Sirtinol 50μM + βHB 5mM
Sirtinol 50μM + NMN 50μM
5 μM
B
Mitochondrial Average Branch Length (PX)
25
20
15
10
5
0
***
Veh
Sirtinol (50μM)
Sirtinol (50μM)+ βHB (5mM)
Sirtinol (50μM)+ NMN (50μM)
C
Mitochondrial Dynamics (% Cells)
100
80
60
40
20
0
Intermediate
Fragmented
Fused
***
***
***
Veh
Sirtinol (50μM)
Sirtinol (50μM)+ βHB (5mM)
Sirtinol (50μM)+ NMN (50μM)

Figure 5

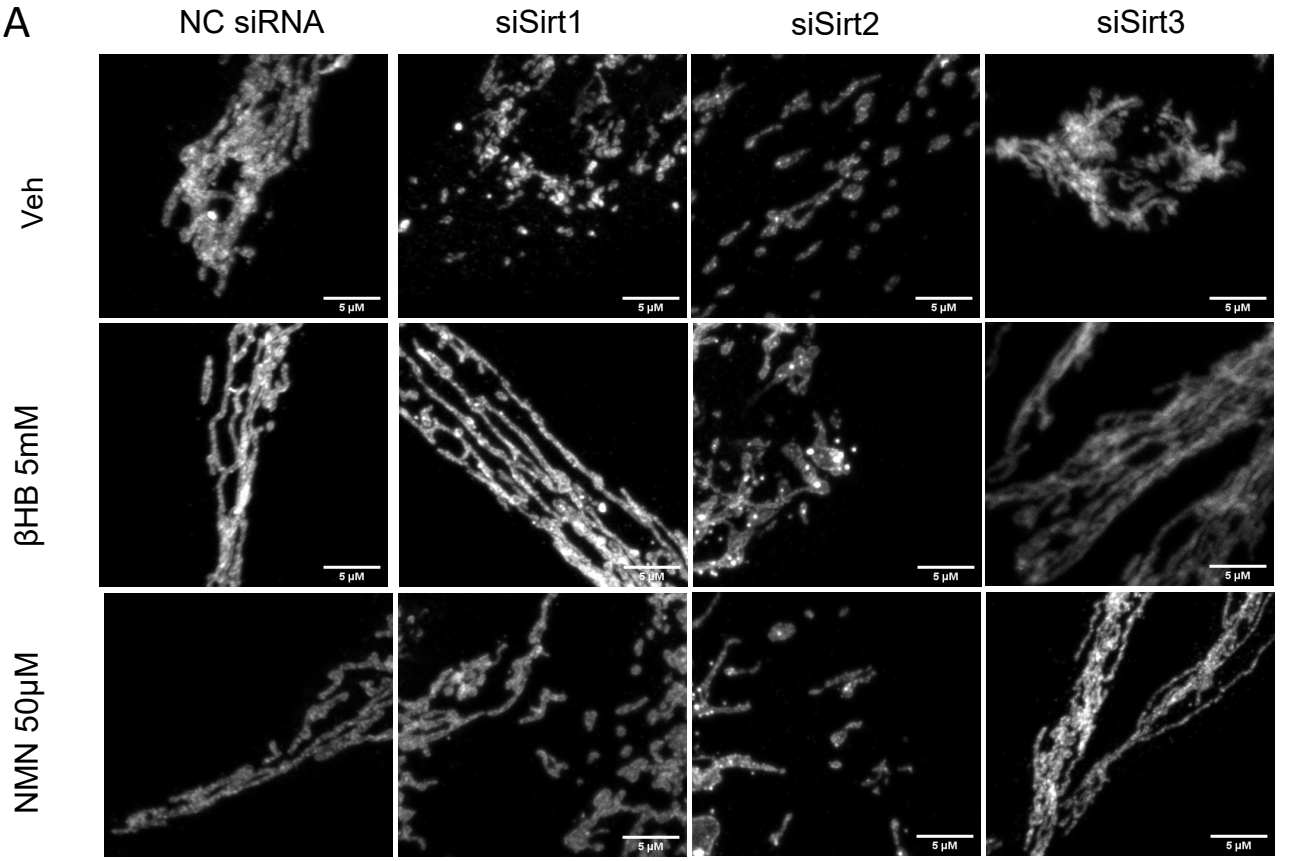
A
NC siRNA
siSirt1
siSirt2
siSirt3
Veh
βHB 5mM
NMN 50μM
5 μM

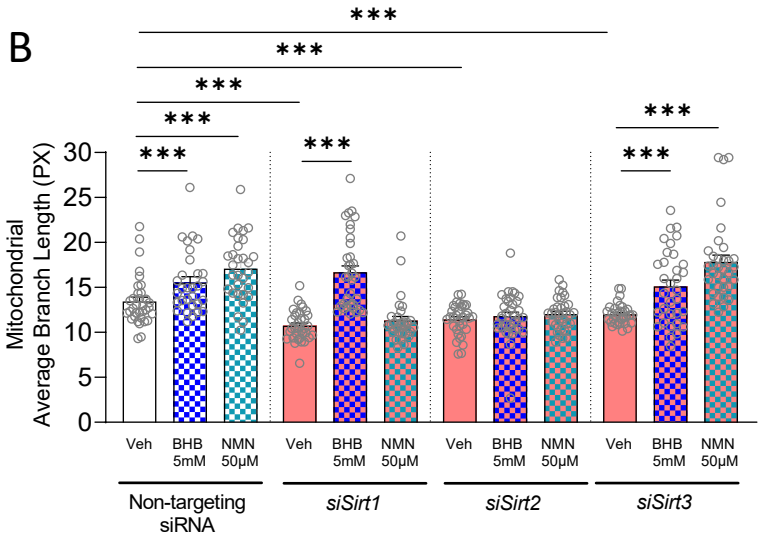
B
Mitochondrial Average Branch Length (PX)
0
5
10
15
20
25
30
***
Veh
BHB 5mM
NMN 50μM
Non-targeting siRNA
siSirt1
siSirt2
siSirt3

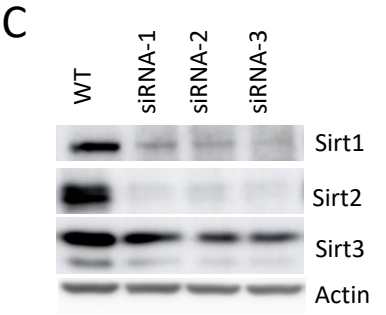
C
WT
siRNA-1
siRNA-2
siRNA-3
Sirt1
Sirt2
Sirt3
Actin

Figure 6

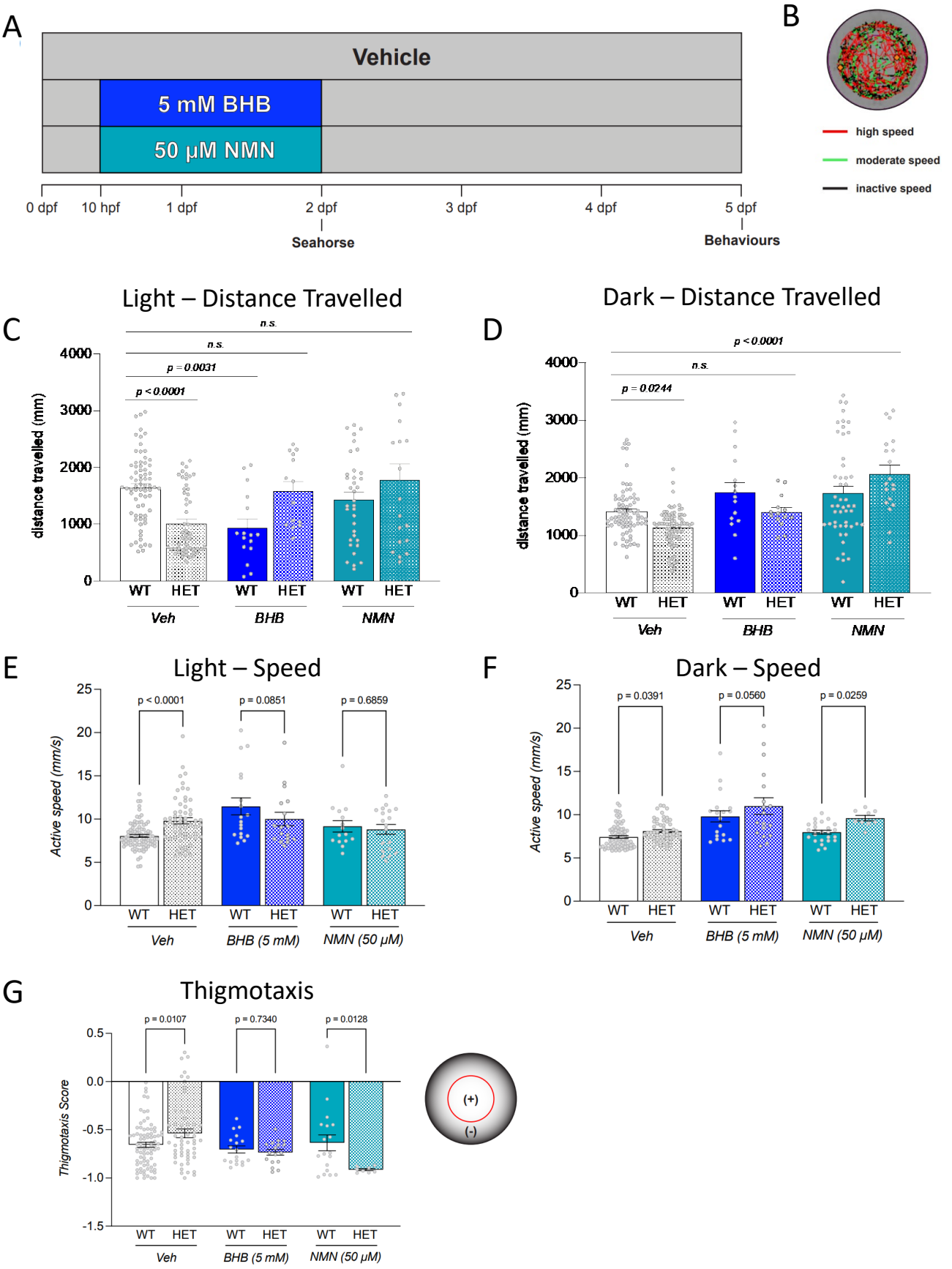
A
Vehicle
5 mM BHB
50 μM NMN
0 dpf
10 hpf
1 dpf
2 dpf
3 dpf
4 dpf
5 dpf
Seahorse
Behaviours
B
high speed
moderate speed
inactive speed
Light – Distance Travelled
C
n.s.
n.s.
p = 0.0031
p < 0.0001
distance travelled (mm)
WT HET WT HET WT HET
Veh BHB NMN
Dark – Distance Travelled
D
p < 0.0001
n.s.
p = 0.0244
distance travelled (mm)
WT HET WT HET WT HET
Veh BHB NMN
Light – Speed
E
p < 0.0001
p = 0.0851
p = 0.6859
Active speed (mm/s)
WT HET WT HET WT HET
Veh BHB (5 mM) NMN (50 μM)
Dark – Speed
F
p = 0.0391
p = 0.0560
p = 0.0259
Active speed (mm/s)
WT HET WT HET WT HET
Veh BHB (5 mM) NMN (50 μM)
Thigmotaxis
G
p = 0.0107
p = 0.7340
p = 0.0128
Thigmotaxis Score
WT HET WT HET WT HET
Veh BHB (5 mM) NMN (50 μM)
(+)
(-)

Figure 7

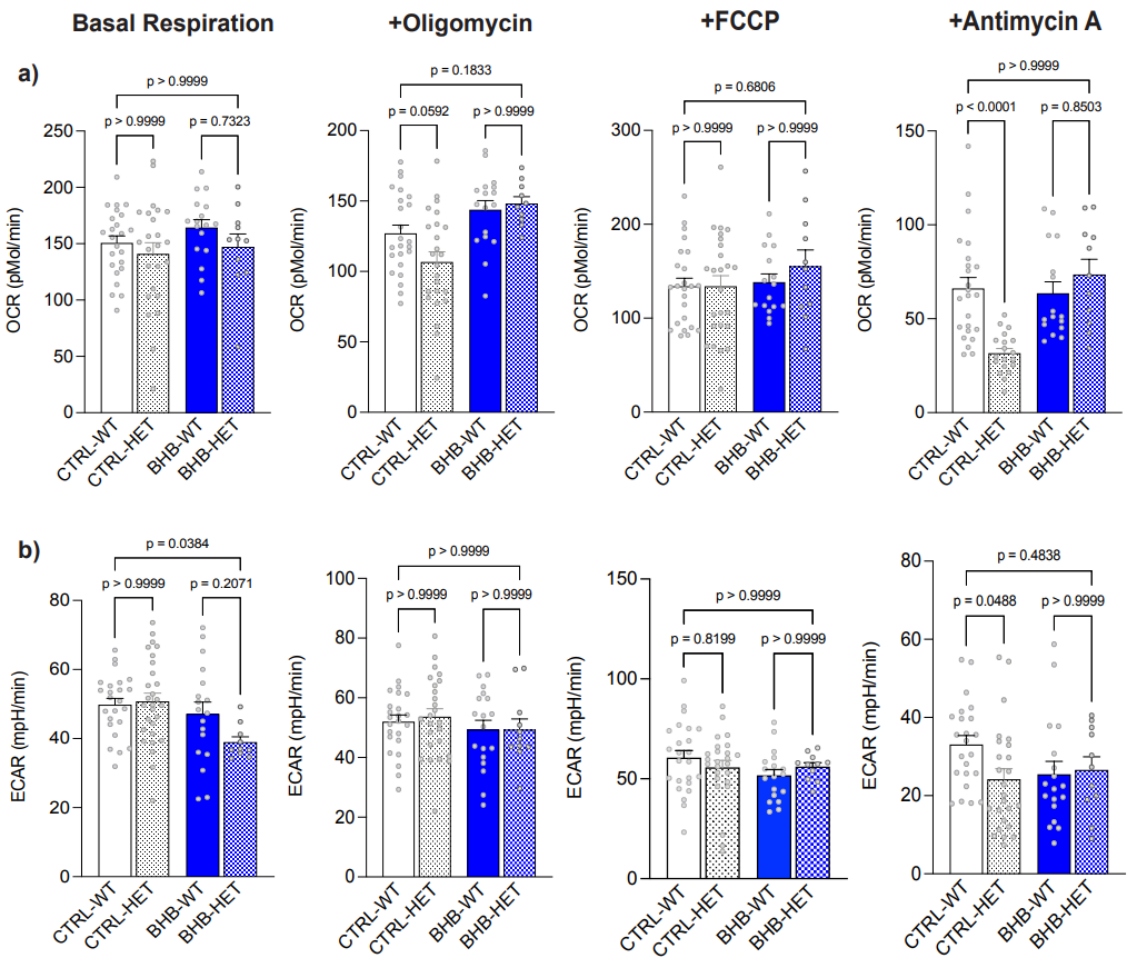
Basal Respiration
+Oligomycin
+FCCP
+Antimycin A
a)
OCR (pMol/min)
p > 0.9999
p > 0.9999
p = 0.7323
p = 0.1833
p = 0.0592
p > 0.9999
p = 0.6806
p > 0.9999
p > 0.9999
p > 0.9999
p < 0.0001
p = 0.8503
CTRL-WT
CTRL-HET
BHB-WT
BHB-HET
b)
ECAR (mpH/min)
p = 0.0384
p > 0.9999
p = 0.2071
p > 0.9999
p > 0.9999
p > 0.9999
p > 0.9999
p = 0.8199
p > 0.9999
p = 0.4838
p = 0.0488
p > 0.9999